Gravity recovery using COSMIC GPS data: application of orbital perturbation theory

C. Hwang

Department of Civil Engineering, National Chiao Tung University, 1001 Ta Hsueh Road, Hsinchu 300, Taiwan
e-mail: hwang@geodesy.cv.nctu.edu.tw; Tel.: +886-3-5724739; Fax: +886-3-5716257

Abstract. COSMIC is a joint Taiwan–US mission to study the atmosphere using the Global Positioning System (GPS) occultation technique. Improved formulas are developed for the radial, along-track, and cross-track perturbations, which are more accurate than the commonly used order-zero formulas. The formulas are used to simulate gravity recovery using the geodetic GPS data of COSMIC in the operational phase. Results show that the EGM96 model can be improved up to degree 26 using 1 year of COSMIC data. TOPEX/POSEIDON altimeter data are used to derive a temporal gravity variation. COSMIC cannot reproduce this gravity variation perfectly because of data noise and orbital configuration, but the recovered field clearly shows the gravity signature due to mass movement in an El Niño.

Key words: COSMIC – GPS – Orbit perturbation – Temporal gravity variation – El Niño

1 Introduction

The Constellation Observing System for Meteorology, Ionosphere, and Climate (COSMIC) is a joint Taiwan (ROC)–US satellite mission to study atmosphere using the Global Positioning System (GPS) occultation technique. This mission is to be launched in 2004 and will deploy a constellation of eight micro-satellites, each equipped with one GPS receiver and two antennas. One antenna is to receive occulted signals for atmospheric study, and the other un-occulted signals for precise orbit determination (POD) (Kuo and Lee 1999). Although the COSMIC mission is primarily for atmospheric research, its POD GPS data can be used for geodetic research. In the early, geodetic phase of COSMIC, selected satellites will fly in tandem mode at altitudes ranging from 300 to 700 km. When using the GPS data in the tandem mode the effect of non-conservative forces can be significantly reduced because of the common mode cancellation. In a simulation study Chao et al. (2000) show that the COSMIC GPS data from the geodetic phase can improve the accuracy of the EGM96 model (Lemoine et al. 1998) for harmonic coefficients up to degree 40 and for selected terms of higher degrees and orders. Other satellite missions equipped with GPS receivers for atmospheric study are, for example, UCAR's (University Corporation for Atmospheric Research) MicroLab-1 and Germany's CHAMP missions; see also Yunck et al. (2000) for a history of GPS sounding of the atmosphere. In particular, CHAMP was launched in July 2000 and it is also equipped with an accelerometer that measures its surface perturbing forces. Thus, compared to COSMIC, the problem of modeling surface forces for CHAMP is substantially ameliorated. CHAMP will not only provide real GPS data for testing the methods developed in this paper, but also improve COSMIC's data coverage for gravity recovery, especially for the polar gap problem.

The geodetic phase of COSMIC will last for less than 1 year and the mission will soon be shifted to the operational phase. Table 1 lists orbital characteristics of COSMIC satellites in the operational phase, which are largely based on Kuo and Lee (1999). The 80° inclination of COSMIC is not officially determined, but any inclination less than 80° will introduce significant polar gaps in the data coverage and will not be ideal for global gravity recovery. In comparison, the GRACE and GOCE missions have polar and nearly polar orbits that will give a better data coverage (Balmino et al. 1998). At an altitude of 800 km, the gravity content sensible to the COSMIC satellites will drop to about harmonic degree 50 (Hwang and Lin 1998), so the data from the operational phase cannot produce high-frequency gravity information. Unlike the study of Chao et al. (2000), in this paper we will use the COSMIC GPS data from the operational phase for gravity recovery. Since the operational phase has a lifetime of 5 years, it will be possible to see the time variation of gravity field with the COSMIC GPS data. The COSMIC orbit is nearly circular; thus, given the GPS-derived positional data of COSMIC satellites, it is convenient to use the linear

Table 1. Orbital characteristics of COSMIC mission in the operational phase

Number of satellites	8
Inclination	80°
Altitude	800 km
Eccentricity	≈ 0
Orbital period	101 minutes
Number of orbital planes	8
Nodal period	314 days
Lifetime	5 years

orbital perturbation theory of Kaula (1966) for gravity computation as in satellite altimetry research; see, for example, Engelis (1987) and Hwang (1995). Kaula's theory is for the general case; in this study, perturbation formulas in the radial, along-track, and cross-track directions will be needed. Such formulas can be derived from Kaula's theory, and formulas of various accuracies have been given by, for example, Schrama (1991) and Rosborough and Tapley (1987). We will first derive improved perturbation formulas with the aim of increasing efficiency and accuracy. The accuracy of the formulas will then be assessed. Finally, these formulas will be used to compute the Earth's gravity field from the COSMIC positional data in various simulations. We will pay a special attention to recovering a time-varying gravity field due to oceanic mass movement derived from TOPEX/POSEIDON (T/P) altimeter data.

2 Methods and data type for gravity recovery from COSMIC

The primary purpose of this study is to recover, by simulations, the geopotential coefficients, $\bar{C}_{nm}$ and $\bar{S}_{nm}$, in the spherical harmonic representation of the Earth's gravitational potential

$$V(r, \phi, \lambda) = \frac{GM}{r} \left[1 + \sum_{n=2}^{\infty} \left(\frac{a_e}{r} \right)^n \sum_{m=0}^{n} (\bar{C}_{nm} \cos m\lambda + \bar{S}_{nm} \sin m\lambda) \bar{P}_{nm}(\sin \phi) \right]$$
$$= \frac{GM}{r} + R \tag{1}$$

where R is the perturbing potential, GM is the product of Newton's gravitational constant and the Earth's mass, (r, ϕ, λ) are the spherical coordinates (radial distance, geocentric latitude, and longitude), a_e is the semi-major axis of the Earth's reference ellipsoid, and $\bar{P}_{nm}$ is the fully normalized Legendre function of degree n and order m (Heiskanen and Moritz 1985). The coordinate system is assumed to be geocentric, so the degree one terms are absent in Eq. (1). There are several methods for recovering the geopotential coefficients from COSMIC GPS data. For example, Fig. 1 shows three possible methods of recovery, as well as applications of global gravity in engineering, oceanography, geophysics, and other disciplines. In one method, called the "dynamic method", we can treat carrier phases and pseudoranges of GPS just

like such regular satellite tracking data as ranges from satellite laser ranging (SLR) and Doppler data from DORIS. Then, with sophisticated software for orbit determination, for example, NASA's GEODYN (Pavlis et al. 1996), we can solve for the geopotential coefficients, as well as the parameters of other perturbing forces and the initial state vectors. The satellite orbit dynamics are needed in this approach; see for example Rim et al. (1996). Another method, called the "kinematic method", uses GPS software to determine the precise positions of the COSMIC satellites without using satellite dynamics. The satellite position is a function of the perturbing forces acting on the satellite, including the force due to the geopotential. Using a linear orbital perturbation theory that links the satellite position to the geopotential, we can estimate the geopotential coefficients. In this kinematic method, the effect of the non-geopotential perturbing forces can be reduced by using a priori force models and further absorbed by an empirical formula (see below). The third method in Fig. 1 first computes the GPS phase accelerations (Jekeli and Garcia 1996), which are then used to compute satellite accelerations. Like satellite position, satellite acceleration is also a function of the geopotential, and in the rectangular coordinates the function is simply

$$\begin{pmatrix} a_x \\ a_y \\ a_z \end{pmatrix} = \nabla V = \begin{pmatrix} \frac{\partial V}{\partial x} \\ \frac{\partial V}{\partial y} \\ \frac{\partial V}{\partial z} \end{pmatrix} \tag{2}$$

where the acceleration components on the left-hand side are computed from the GPS phases and the expressions of the gradient components of V can easily be derived from Eq. (1) with a suitable coordinate transformation. Equation (2) establishes the linear relationships between the observables (i.e. the accelerations), and the parameters (i.e. the geopotential coefficients). However, the GPS-derived acceleration is again a combination of all perturbing forces, so a priori force models are needed to obtain the "pure" acceleration due to the geopotential.

Considering the limitations of our facility, in this study we will use the positional data of COSMIC to recover gravity, i.e., we will use the kinematic approach. The use of positional data from GPS-tracked satellites for gravity recovery has been recommended by, for example, Schrama (1991) and Balmino et al. (1998). Like radial ranges from satellite altimetry, positional data of COSMIC can be used for gravity recovery, but there are two major differences: (1) COSMIC positional data are three-dimensional, while altimeter ranges are one-dimensional, and (2) gravity recovery with altimeter ranges is affected by the dynamic oceanic topography, while COSMIC data are free from this effect. In addition, altimetry yields gravity only over the oceans, but with a much higher resolution, and it does not require downward continuation. Furthermore, the GPS POD data of COSMIC will be sampled at 1 Hertz (Kuo and Lee 1999), which far exceeds the necessary sampling rate at the 800-km altitude. Thus the positional data of COSMIC can be re-sampled at a lower rate, for example,
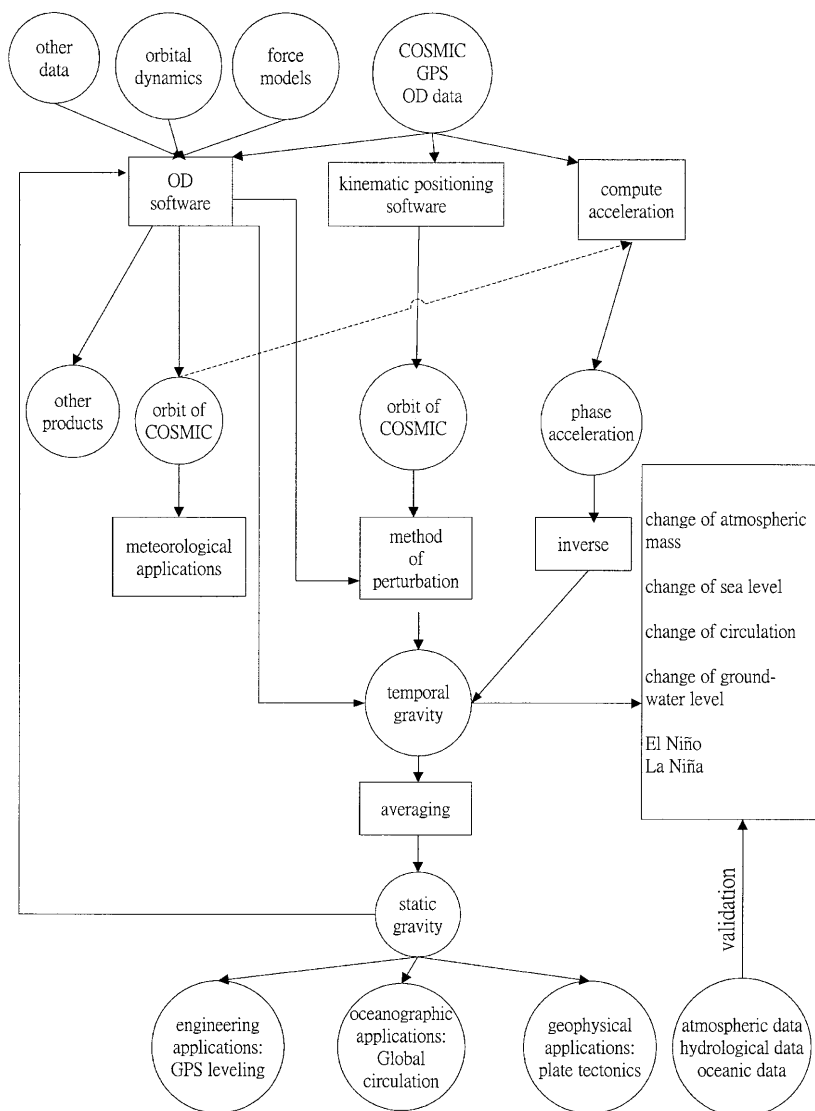
Fig. 1. Three methods of gravity recovery from COSMIC GPS data and applications of gravity

a 1-minute interval, that is comparable with the shortest wavelength of gravity signal that can be sensed by the COSMIC satellites. In the case of 1-minute normal points, the accuracy of the positions of COSMIC can be far better than the 10-cm accuracy of the GPS-determined T/P orbit (Bertiger et al. 1994). For example, Schrama (1991) and Balmino et al. (1998) assume a 3-cm standard deviation for the GPS-determined positions in their simulations for the GOCE mission. By the year 2004 the accuracy of GPS-determined orbit will surely be further improved.

3 Orbital perturbations due to the geopotential

3.1 Radial, along-track, and cross-track perturbations

In order to use the positional data of COSMIC, we will need to know the linear relationship between COSMIC's position and the geopotential coefficients. Such a relationship can be established using Kaula's theory of linear perturbations of the six Keplerian elements, whose notations are as follows:

a semi-major axis of osculating orbital ellipse
e eccentricity of osculating orbital ellipse
I inclination
ω argument of perigee
Ω right ascension of the ascending node
M mean anomaly

Given the three-dimensional, positional data of COSMIC, the analytical expressions for positional perturbations in the radial, along-track, and cross-track directions are needed and are derived below. First, the radial distance from the geocenter to the satellite can be expressed as

$$r = a(1 - e\cos E) \tag{3}$$

where E is the eccentricity anomaly. The radial perturbation is then

$$\Delta x_1 = \frac{\partial r}{\partial a}\Delta a + \frac{\partial r}{\partial e}\Delta e + \frac{\partial r}{\partial E}\Delta E$$
$$= (1 - e\cos E)\Delta a - (a\cos E)\Delta e + (ae\sin E)\Delta E \tag{4}$$

Furthermore, as shown in Fig. 2, the along-track and cross-track perturbations can be expressed as
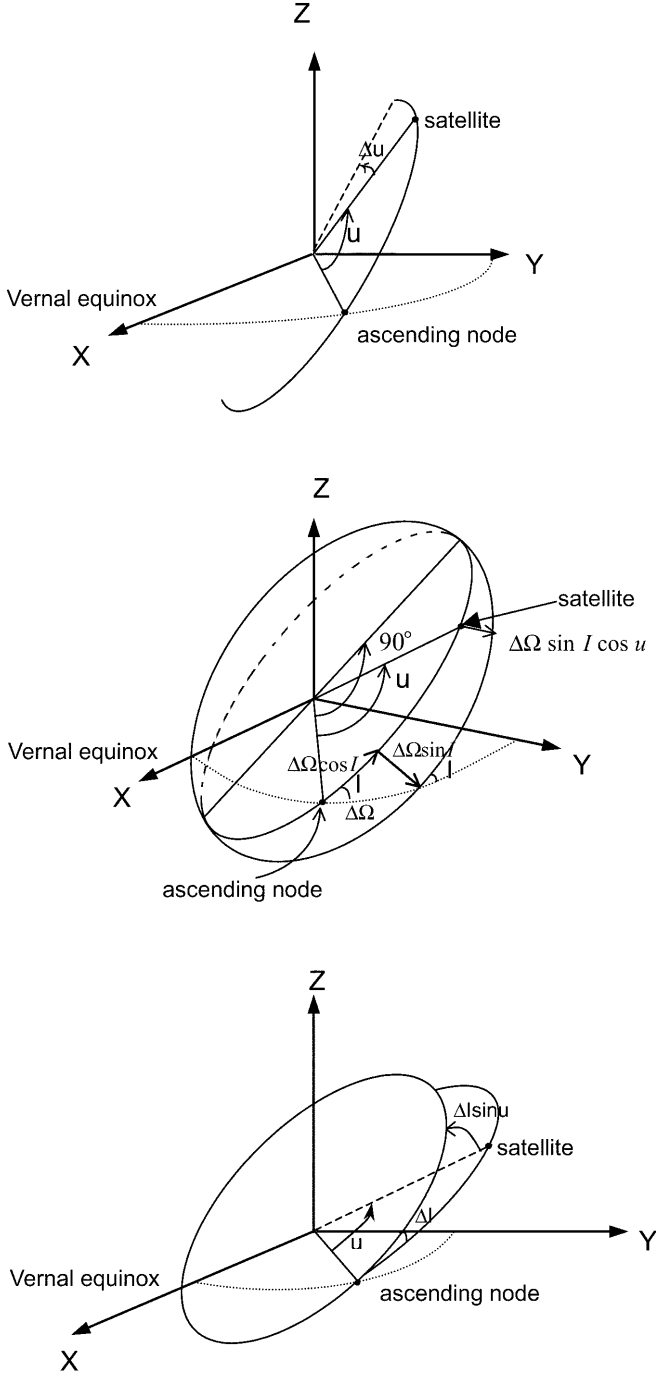
Fig. 2. Geometry showing the effects of the perturbations in argument of perigee (**top**), right ascension of the ascending node (**center**) and inclination (**bottom**) on the radial, along-track, and cross-track perturbations of satellite position

$$\Delta x_2 = r(\Delta u + \Delta \Omega \cos I) = r[\Delta \omega + \Delta f + (\cos I)\Delta\Omega] \quad (5)$$

$$\Delta x_3 = r[(\sin u)\Delta I - (\sin I \cos u)\Delta\Omega] \quad (6)$$

where f is true anomaly and $u = \omega + f$ is argument of latitude. The perturbations in Eqs. (4), (5), and (6) are already expressed in terms of the perturbations of the Keplerian elements, except for Δf and ΔE. Complicated expressions for Δf and ΔE in terms of Keplerian

perturbations using infinite series expansions can be found in Rosborough and Tapley (1987). Because the sole purpose of the perturbation formulas is to serve as the linear functions for computing the design matrix in estimating the geopotential coefficients (see below), it will be possible to use simplified, rigorous expressions of perturbations that are free from infinite series expansions. First, the following relationships hold:

$$M = E - e \sin E \quad (7)$$

$$\cos f = \frac{\cos E - e}{1 - e\cos E}, \quad \sin f = \frac{\sqrt{1 - e^2} \sin E}{1 - e\cos E} \quad (8)$$

From Eq. (7), we have

$$\begin{aligned}\Delta M &= \frac{\partial M}{\partial E}\Delta E + \frac{\partial M}{\partial e}\Delta e \\ &= (1 - e\cos E)\Delta E - (\sin E)\Delta e\end{aligned} \quad (9)$$

Re-arranging Eq. (9), we obtain

$$\Delta E = \frac{1}{1 - e\cos E}\Delta M + \frac{\sin E}{1 - e\cos E}\Delta e \quad (10)$$

Using a similar derivation, we have from Eq. (8)

$$\begin{aligned}\Delta f &= \frac{\sqrt{1 - e^2}}{1 - e\cos E}\Delta E + \frac{\sin E}{\sqrt{1 - e^2}(1 - e\cos E)}\Delta e \\ &= \frac{\sqrt{1 - e^2}}{(1 - e\cos E)^2}\Delta M + \frac{(2 - e^2 - e\cos E)\sin E}{\sqrt{1 - e^2}(1 - e\cos E)^2}\Delta e\end{aligned} \quad (11)$$

Let Δs_k, $k = 1,\ldots,6$, be the perturbations of the six Keplerian elements in the order a, e, I, Ω, ω, and M. Substituting Eqs. (10) and (11) into Eqs. (4), (5), and (6), we have

$$\Delta x_i = \sum_{k=1}^{6} c_k^i \Delta s_k \quad i = 1, 2, 3 \quad (12)$$

where the coefficients are

$$c_3^1 = c_4^1 = c_5^1 = 0, \quad c_1^1 = 1 - e\cos E,$$

$$c_2^1 = -a\cos E + \frac{ae\sin^2 E}{1 - e\cos E}, \quad c_6^1 = \frac{ae\sin E}{1 - e\cos E}$$

$$c_1^2 = c_3^2 = 0, \quad c_2^2 = \frac{r(2 - e^2 - e\cos E)\sin E}{\sqrt{1 - e^2}(1 - e\cos E)^2},$$

$$c_4^2 = r\cos I, \quad c_5^2 = r, \quad c_6^2 = \frac{r\sqrt{1 - e^2}}{(1 - e\cos E)^2} \quad (13)$$

$$c_1^3 = c_2^3 = c_5^3 = c_6^3 = 0,$$

$$c_3^3 = \frac{r[\sin\omega(\cos E - e) + \sqrt{1 - e^2}\cos\omega\sin E]}{1 - e\cos E}$$

$$c_4^3 = r\sin I \frac{\left[\cos\omega(\cos E - e) - \sqrt{1 - e^2}\sin\omega\sin E\right]}{1 - e\cos E}$$

In Eqs. (13), E is simply computed iteratively from M and e by Eq. (7) without using infinite series expansions,

and r is computed from a, e, and E by Eq. (3). The perturbations in the Keplerian elements, Δs_k, can be obtained by integrating Lagrange's equations of motion about a reference orbit that has fixed a, e, and I and linearly precessing Ω, ω, and M (Kaula 1966; Balmino 1994). For later development, the expressions of Δs_ks are now briefly discussed. First, considering satellite altitude and orbital eccentricity, we can express the perturbing potential R in Eq. (1) as a function of the Keplerian elements in a truncated series

$$R = \sum_{n=2}^{K} \sum_{m=0}^{n} \sum_{p=0}^{n} \sum_{q=-Q}^{Q} R_{nmpq} \tag{14}$$

where K is the maximum degree of the spherical harmonic expansion depending on the satellite altitude, and Q is a number that depends on the orbital eccentricity. For example, at an altitude of 800 km, K can be 50, and for a nearly circular orbit Q can be 1; see also the discussion in Balmino (1994). Furthermore

$$R_{nmpq} = \frac{GM a_e^n}{a^{n+1}} \bar{F}_{nmp}(I) G_{npq}(e) S_{nmpq}(\omega, M, \Omega, \theta) \tag{15}$$

where

$$\begin{aligned}
&S_{nmpq}(\omega, M, \Omega, \theta) \\
&= \begin{pmatrix} \bar{C}_{nm}^+ \\ -\bar{S}_{nm}^- \end{pmatrix} \cos[(n-2p)\omega + (n-2p+q)M \\
&\quad + m(\Omega - \theta)] + \begin{pmatrix} \bar{S}_{nm}^+ \\ \bar{C}_{nm}^- \end{pmatrix} \sin[(n-2p)\omega \\
&\quad + (n-2p+q)M + m(\Omega - \theta)]
\end{aligned} \tag{16}$$

and θ is Greenwich sidereal time; $\bar{C}_{nm}^+$ and $\bar{S}_{nm}^+$ are fully normalized spherical harmonic coefficients [see Eq. (1)] when $(n-m)$ is even, and $\bar{C}_{nm}^-$ and $\bar{S}_{nm}^-$ are such coefficients when $(n-m)$ is odd. $\bar{F}_{nmp}$ is the fully normalized inclination function and $G_{npq}(e)$ is the eccentricity function; see Kaula (1966) and Heiskanen and Moritz (1985). The normalizing factor for $\bar{F}_{nmp}$ is exactly the same as the normalizing factor for $\bar{P}_{nm}$. Use of $\bar{F}_{nmp}$ is compatible with the use of normalized geopotential coefficients in Eq. (1). Let

$$\begin{aligned}
&S_{nmpq}^*(\omega, M, \Omega, \theta) \\
&= \begin{pmatrix} \bar{C}_{nm}^+ \\ -\bar{S}_{nm}^- \end{pmatrix} \sin[(n-2p)\omega + (n-2p+q)M \\
&\quad + m(\Omega - \theta)] - \begin{pmatrix} \bar{S}_{nm}^+ \\ \bar{C}_{nm}^- \end{pmatrix} \cos[(n-2p)\omega \\
&\quad + (n-2p+q)M + m(\Omega - \theta)]
\end{aligned} \tag{17}$$

Then the perturbations in a, e, and I are

$$\Delta s_i = \sum_{n=2}^{K} \sum_{m=0}^{n} \sum_{p=0}^{n} \sum_{q=-Q}^{Q} \alpha_{nmpq}^i S_{nmpq} \tag{18}$$

and the perturbations in Ω, ω, and M are

$$\Delta s_i = \sum_{n=2}^{K} \sum_{m=0}^{n} \sum_{p=0}^{n} \sum_{q=-Q}^{Q} \alpha_{nmpq}^i S_{nmpq}^* \tag{19}$$

The coefficients α_{nmpq}^i in the order $a, e, I, \Omega, \omega,$ and M are as follows:

$$\alpha_{nmpq}^1 = 2ab\bar{F}_{nmp}G_{npq}(n-2p+q)$$

$$\begin{aligned}
\alpha_{nmpq}^2 &= b\frac{(1-e^2)^{1/2}}{e}\bar{F}_{nmp}G_{npq} \\
&\quad \times [(1-e^2)^{1/2}(n-2p+q) - n + 2p]
\end{aligned}$$

$$\alpha_{nmpq}^3 = b\bar{F}_{nmp}G_{npq}\frac{[(n-2p)\cos I - m]}{\sin I(1-e^2)^{1/2}}$$

$$\alpha_{nmpq}^4 = b\frac{\bar{F}'_{nmp}G_{npq}}{\sin I(1-e^2)^{1/2}}$$

$$\begin{aligned}
\alpha_{nmpq}^5 &= b\left[\frac{(1-e^2)^{1/2}}{e}\bar{F}_{nmp}\bar{G}'_{npq}\right. \\
&\quad \left. -\frac{\cos I}{\sin I(1-e^2)^{1/2}}\bar{F}'_{nmp}G_{npq}\right]
\end{aligned} \tag{20}$$

$$\begin{aligned}
\alpha_{nmpq}^6 &= b\bar{F}_{nmp}\left[2(n+1)G_{npq} - \frac{(1-e^2)^{1/2}}{e}G'_{npq}\right. \\
&\quad \left. -3G_{npq}(n-2p+q)\frac{\bar{n}}{\dot{\psi}_{nmpq}}\right]
\end{aligned}$$

where

$$b = \frac{\bar{n}}{\dot{\psi}_{nmpq}}\left(\frac{a_e}{a}\right)^n \tag{21}$$

$$\bar{n} = \sqrt{\frac{GM}{a^3}} \tag{22}$$

$$\dot{\psi}_{nmpq} = (n-2p)\dot{\omega} + (n-2p+q)\dot{M} + m(\dot{\Omega} - \dot{\theta}) \tag{23}$$

$$\bar{F}'_{nmp} = \frac{\partial \bar{F}_{nmp}}{\partial I}, \quad G'_{npq} = \frac{\partial G_{npq}}{\partial e} \tag{24}$$

In Eq. (23), $\dot{\theta}$ is the speed of the Greenwich sidereal time, which is about the Earth's mean rotational rate (7.292115×10^{-5} rad s^{-1}) and the precessing rates $\dot{\omega}$, $\dot{M}$, and $\dot{\Omega}$ are computed by

$$\dot{\Omega} = \frac{3\bar{n}C_{20}a_e^2}{2(1-e^2)^2 a^2}\cos^2 I$$

$$\dot{\omega} = \frac{3\bar{n}C_{20}a_e^2}{4(1-e^2)^2 a^2}(1 - 5\cos^2 I) \tag{25}$$

$$\dot{M} = \bar{n} - \frac{3\bar{n}C_{20}a_e^2}{4(1-e^2)^{3/2} a^2}(3\cos^2 I - 1)$$

where C_{20} is the second-degree zonal harmonic (about -0.00108263). The perturbation in mean anomaly, ΔM, has taken into account the variation in M due to the

change in the mean motion arising from the perturbation of the semi-major axis [the third term in Eqs. (20)]; see also Kaula (1966, p 49). Including this second-order effect will improve the accuracy of the along-track perturbation model.

In the practical computations, each of the three positional perturbations can be represented as the inner product of two vectors:

$$\Delta x_i = \mathbf{A}_i^T \boldsymbol{\beta} \qquad (26)$$

where $\boldsymbol{\beta}$ is a vector containing the geopotential coefficients and $\mathbf{A}_i$ is a vector obtained by combining Eqs. (12), (18), and (19). For an orbital arc shorter than about 1 week, the a, e, and I elements in α^i_{nmpq} can be regarded as constants, so we can compute α^i_{nmpq} only once for all terms up to degree K and index Q [see Eq. (14)]. For a nearly circular orbit, approximate analytical expressions of Δx_i can be obtained; see for example Schrama (1991) and Rosborough and Tapley (1987). In particular, for the radial perturbation the so-called "order-zero" perturbation (Rosborough and Tapley 1987) is frequently used in satellite altimetry in connection with orbit refinement and gravity improvement; see for example Wagner (1989), Engelis (1987), and Hwang (1995). The order-zero formulas of Δx_i are derived in Appendix A, and their accuracies will be compared with those of the rigorous formulas given in this section.

As a final note, in all computations below the inclination function is computed by a FORTRAN subroutine "FINCRS" and the eccentricity function by a subroutine "GKAULAF", both supplied by G. Balmino (private communication, 1999); a brief mention of these programs is given by Balmino (1994). In fact, we also use the summation formula given by Kaula (1966, p 34) to compute the inclination function, and the result is identical to that computed by "FINCRS" up to at least harmonic degree 50. In addition, for the order-zero formulas in Appendix A, there is no need to compute the eccentricity function.

3.2 Higher-order and resonance effects

The linear theory described above cannot account for the higher-order perturbations which arise from the interactions between the first-order (linear) perturbations and the Keplerian elements, and the linear theory breaks down in the case of resonance. A detailed derivation of higher-order perturbations can be found in Kaula (1966). However, since the higher-order perturbations are not linear functions of the geopotential coefficients, they are of no use for the gravity computation in this study. Resonance occurs when the frequency $\dot{\psi}_{nmpq}$ in Eq. (21) approaches zero. Depending on the closeness of $\dot{\psi}_{nmpq}$ to zero, there are different degrees of resonance, i.e. shallow, deep, and perfect resonances (Reigber 1989). For COSMIC at the 800-km altitude, we find that if

$$\frac{|\dot{\psi}_{nmpq}|}{\dot{M}} < 0.01 \qquad (27)$$

then the coefficients in Eq. (20) become excessively large and the perturbations computed by Eq. (12) do not agree with those from the direct numerical method (see below). Thus, if the condition in Eq. (27) is met, we simply set $\alpha^i_{nmpq} = 0$. Fortunately, these two effects can be modeled by simple empirical formulas. An empirical formula for the radial perturbation can be found in, for example, Colombo (1984). In this paper, we adopt the following empirical model to account for the higher-order and resonance effects for COSMIC:

$$\Delta x_i^e = a_0^i + a_1^i \cos u + a_2^i \sin u + a_3^i \sin 2u + a_4^i t \cos u$$
$$+ a_5^i t \sin u + a_6^i t^2 \cos u + a_7^i t^2 \sin u + a_8^i t + a_9^i t^2 \qquad (28)$$

where t is the time elapsed since a reference epoch and a_k^i are the coefficients for the ith perturbation component. Note that such an empirical model can also partly absorb the error in the initial state vector and errors in the force models in the parameter estimation involving satellite dynamics. The choice in Eq. (28) is based on the results in Colombo (1984), Engelis (1987), and Hwang (1995), and most importantly, based on the numerical tests carried out in this study.

3.3 Errors of the perturbation formulas

In order to see how the perturbation formulas perform, we can replace the geopotential coefficients in the formulas by the differences between two sets of geopotential coefficients to compute the predicted perturbations along the trajectory of the satellite. In this way the predicted perturbations are in theory the differences between the two satellite trajectories resulting from the use of two different geopotential models in the equations of motion of the satellite. Next, the "true" perturbations can be obtained by differencing the two trajectories computed by strict numerical integrations of equations of motion. For each component the relative error of the perturbation formula is defined as

$$M_e = \frac{\Delta D}{D} \qquad (29)$$

where D is the root-mean-square (RMS) value of the true perturbation, and ΔD is the RMS value of the difference between the true and the predicted perturbations.

We choose the EMG96 and OSU91A geopotential coefficients to form the true and predicted perturbations (actually the trajectory differences). The numerical integrations were carried out using the DVDQ integrator (Krogh 1974); see also Hwang and Lin (1998). Table 2 shows the relative errors and the statistics of the differences between the true and predicted perturbations for three kinds of perturbation formulas: the order-zero formulas in Appendix A, and the perturbation formulas in this paper with $Q = 1$ and $Q = 2$. The arc length for

Table 2. Relative errors of perturbation formulas and statistics of the difference between the true and predicted perturbations

Type of formula	Relative error (%) $(r/a/c)$[a]	Maximum difference (cm) $(r/a/c)$	Minimum difference (cm) $(r/a/c)$	RMS difference (cm) $(r/a/c)$
a To harmonic degree 10, arc length $= 7$ days				
Order-zero	1.08/1.21/0.92	1.1/6.1/0.8	−1.5/−4.6/−1.3	0.4/1.80/0.3
This study, $Q = 1$	0.85/0.64/0.49	1.0/3.3/0.5	−0.8/−2.1/−0.6	0.3/0.9/0.2
This study, $Q = 2$	0.42/0.53/0.49	0.4/2.5/0.5	−0.4/−1.5/−0.6	0.1/0.8/0.2
b To harmonic degree 50, arc length $= 7$ days				
Order-zero	1.52/3.43/3.38	4.6/ 34.8 /10.5	−4.6/−33.9/−7.8	1.3/10.3/2.7
This study, $Q = 1$	1.18/1.10/0.93	3.3/14.5/2.5	−4.1/−12.4/−2.7	1.0/3.5/0.7
This study, $Q = 2$	0.96/1.08/0.93	2.7/9.4/2.5	−2.7/−10.7/−2.7	0.8/3.4/0.7

[a] r = radial, a = along-track, c = cross-track,
Q = upper limit of index in eccentricity function

all cases is 7 days. For each relative error we also experiment with two different expansion degrees: $K = 10$ and $K = 50$. [See Eq. (14) for Q and K]. From Table 2, we find that for all formulas, the relative error increases as K increases. That is, the perturbation formulas are less accurate for a high-degree expansion than for a low one. The largest error is in the along-track component and the smallest error is in the cross-track component. For the along-track component, the case with $Q = 2$ improves the accuracy only marginally compared to the case with $Q = 1$. For all components, changing from $Q = 1$ to $Q = 2$ doubles the computing time. Also, the formulas with $Q = 1$ out-perform the order-zero formulas and require less computing time.

Figure 3 shows the differences between the true perturbation and the predicted perturbations based on the three models, for the radial component and for $K = 50$. The centimeter-level error in the formulas with Q equal to 1 and 2 is considerably smaller than the positional error of COSMIC from GPS. In the differences in the along-track direction, for all formulas there are distinct

components at 0.02 cycles per revolution (cpr) and 2-cpr components of time-dependent amplitude; thus we use the following 15-coefficient empirical model for the along-track component:

$$\Delta x_i^e = a_0^i + a_1^i \cos u + a_2^i \sin u + a_3^i \sin 2u + a_4^i t \cos u$$
$$+ a_5^i t \sin u + a_6^i t^2 \cos u + a_7^i t^2 \sin u + a_8^i t$$
$$+ a_9^i t^2 + a_{10}^i \cos 2u + a_{11}^i t \cos 2u + a_{12}^i t \sin 2u$$
$$+ a_{13}^i \cos 0.02u + a_{14}^i \sin 0.02u \qquad (30)$$

Figure 4 shows the differences in the along-track direction resulting from the uses of the 10-coefficient model [see Eq. (28)] and the 15-coefficient model [see Eq. (30)] in the formulas with $Q = 2$. Clearly, the 10-coefficient model cannot account for the large difference near the end of the arc. Use of the 15-coefficient model reduces the RMS error from 8.3 to 3.4 cm, which is comparable to the assumed positional error of COSMIC. Note that, when estimating geopotential coefficients from the positional data, we can use
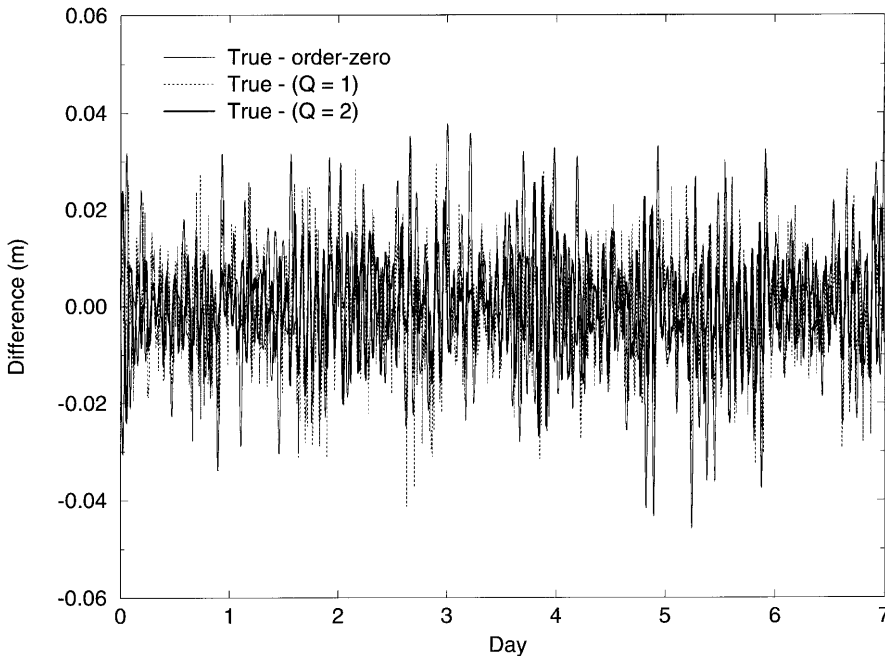

Fig. 3. Differences between the true perturbation, and three predicted perturbations computed with three perturbation models (order-zero, Q = 1 and Q = 2). Day is the number of days elapsed since the first data point
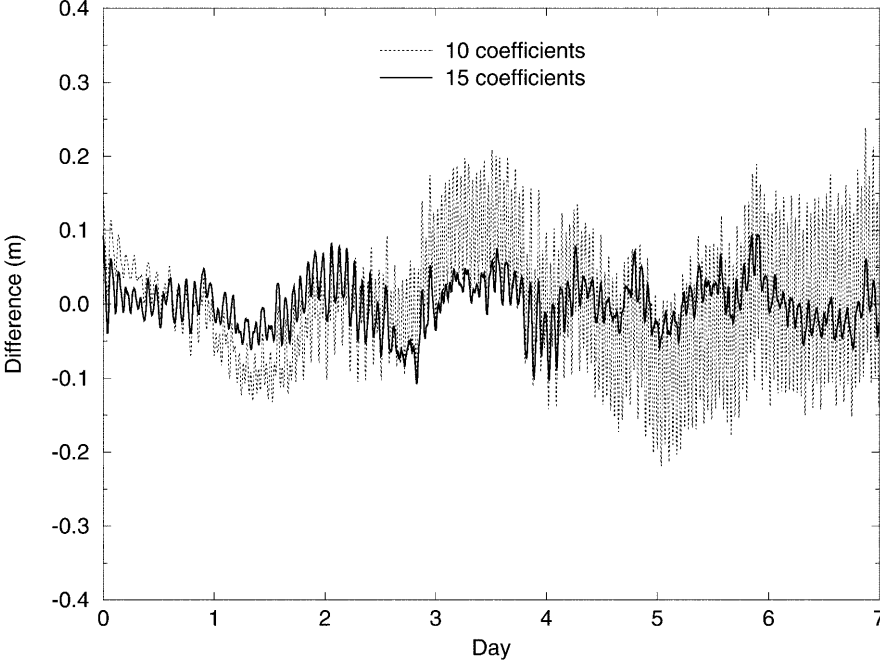
Fig. 4. Difference between the true and predicted along-track perturbations using 10 and 15 coefficients in the empirical model. The perturbation model uses Q = 2. Day is the number of days elapsed since the first data point

iterations to reduce the effect of formula error, because the successively estimated coefficients will become stable and the perturbations will approach zero.

In summary, based on the relative errors in Table 2 and the assumed data noise, we will use the perturbation formulas with $Q = 1$ in all simulations below. The maximum arc length that is considered valid for the reference orbit in the perturbation formulas and the empirical model is 7 days; a longer arc should be divided into multiple 7-day segments with each segment having a new reference orbit and a new set of empirical coefficients.

4 Use of orbital perturbation formulas

The linear perturbation formulas can be used to compute the design matrix when estimating the geopotential coefficients. Given the positional data of COSMIC, at each epoch we can set up observation equations in the radial, along-track, and cross-track directions as

$$x_i + v_i = x_i^0(\boldsymbol{\beta_0}) + \frac{\partial \Delta x_i}{\partial \boldsymbol{\beta}}\bigg|_{\boldsymbol{\beta}=\boldsymbol{\beta_0}} \Delta \boldsymbol{\beta} + \Delta x_i^e(\boldsymbol{\zeta}),$$

$$i = 1, 2, 3 \quad (31)$$

where x_i are the positional data with noise v_i, $\boldsymbol{\beta}$ is a vector containing the geopotential coefficients, $\boldsymbol{\beta_0}$ is an approximation of $\boldsymbol{\beta}$, $\Delta\boldsymbol{\beta}$ is the correction with $\boldsymbol{\beta} = \boldsymbol{\beta_0} + \Delta\boldsymbol{\beta}$, $\boldsymbol{\zeta}$ contains the empirical coefficients and finally x_i^0 is an approximation of x_i. As with gravity refinement using satellite altimeter data, the idea here is to use the so-called residual observations $(x_i - x_i^0)$, where x_i are the positions of COSMIC determined by the kinematic approach using GPS data, and x_i^0 are approximations of x_i that are computed with an a priori geopotential model and other force models. Let

$$\mathbf{X} = \begin{bmatrix} \Delta\boldsymbol{\beta} \\ \boldsymbol{\zeta} \end{bmatrix} \quad (32)$$

Then $\mathbf{X}$ can be solved by the least-squares (LS) method

$$\mathbf{X} = (\mathbf{A}^\mathsf{T}\mathbf{PA} + \mathbf{P_X})^{-1}\mathbf{A}^\mathsf{T}\mathbf{PL} \quad (33)$$

where $\mathbf{A}$ is the design matrix composed of $(\partial \Delta x_i)/(\partial \boldsymbol{\beta})$ and the function values of the empirical model; vector $\mathbf{L}$ contains the residual observations, i.e. $x_i - x_i^0$; $\mathbf{P}$ is the weight matrix of $\mathbf{L}$; and $\mathbf{P_X}$ is the a priori weight matrix of $\mathbf{X}$. As in standard practice, we have $\mathbf{P} = \mathrm{diag}(1/e_1^2, \ldots, 1/e_k^2)$, where $e_1, \ldots, e_k$ are the standard deviations of the observations (the positional data of COSMIC determined from GPS) and k is the number of observations. Assuming that the variances of the geopotential coefficients follow the modified Kaula rule (Reigber 1989), i.e.

$$\bar{\sigma}_n^2 = \frac{1}{2n+1}\sum_{m=0}^{n}(\bar{C}_{nm}^2 + \bar{S}_{nm}^2) \approx 5 \times 10^{-11}n^{-4} \quad (34)$$

then symbolically $\mathbf{P_X} = \mathrm{diag}(P_{c_{nm}}, P_{s_{nm}}, 0)$ (the weights of the empirical coefficients are zeros) is a diagonal matrix with its elements computed by

$$P_{c_{nm}} = P_{s_{nm}} = \frac{1}{\bar{\sigma}_n^2} \quad (35)$$

Use of $\mathbf{P_X}$ is necessary for data of non-global coverage, especially when solving high-degree terms and/or using sparse data. Furthermore, according to Wagner (1989, pp 293–296), the zonal terms will result in 1-cpr radial orbit perturbation (also the along-track and cross-track perturbations, but not shown by Wagner). The empirical models in Eqs. (28) and (30) also explicitly contain the 1-cpr variation of orbit. Thus the 1-cpr perturbations are doubly counted by the zonal terms and the empirical

terms. The 1-cpr term will not cause problems in accurately modeling the orbit perturbations, as demonstrated by the high accuracies of the perturbation and empirical formulas in Table 2. However, the 1-cpr term will indeed cause difficulty in estimating the zonal terms from the positional data of COSMIC. Using the a priori weight matrix $\mathbf{P_X}$ can mitigate such difficulty: the weight matrix helps to separate the zonal terms from the empirical models when solving the geopotential coefficients from the positional data (see below). More discussion on using weighted constraints in geopotential estimation from satellite tracking data can be found in, for example, Reigber (1989).

In this method it is clear that accurate modeling of the non-geopotential perturbing forces for x_i^0 is crucial to the success of recovering gravity. To give an example of how well perturbing forces could be modeled in the 1990s, consider the orbit determination result of T/P: Tapley et al. (1994) estimate that the major perturbing forces can be so well modeled that the total contribution of the mismodeled forces to T/P radial orbit error is about the assumed noise level of COSMIC data in this paper, i.e. 3 cm. Furthermore, Cheng and Tapley (1999), Chen et al. (1999), and Nerem et al. (2000) show that the time variations of some low-degree harmonics and the geocenter can be determined with sufficient accuracy using SLR data. In their works the non-geopotential perturbing forces can be well modeled so that their residual errors do not alias into the time-varying signals they wish to recover. Given the many years of force model improvement before the launch of COSMIC, particularly that made for CHAMP and GRACE (the CHAMP and GRACE altitudes are even lower than COSMIC's), the effect of mismodeled perturbing forces on the COSMIC orbit will be reduced to the T/P level or smaller. Also, the empirical formulas will absorb the long-wavelength part of the mismodeled perturbing forces.

5 Simulations of gravity recovery from COSMIC data

5.1 Improving current gravity models

Here we wish to see how current gravity models, especially the EGM96 model, can be improved using the positional data of COSMIC. The steps of simulation are as follows.

(1) Integrate a 7-day orbit at a 1-minute interval using the EGM96 coefficients for each of the eight COSMIC satellites. Random errors are added to the orbits based on a 3-cm standard deviation in GPS positioning. These orbits are treated as the positional data of COSMIC.

(2) Repeat (1), but with the OSU91A coefficients and without random errors. These orbits are treated as approximate orbits based on a priori geopotential coefficients (in this case, OSU91A).

(3) Subtract the orbits in (2) from the orbits in (1) to obtain the radial, along-track, and cross-track perturbations.

(4) Estimate the differences between the EGM96 and OSU91A coefficients by LS using the linear perturbation theory with data from the "observed" perturbations in step (3).

At the initial epoch of integrations, the right ascensions of orbital planes and arguments of latitudes of the eight satellites in the COSMIC constellation are as shown in Fig. 5. The amount of data to process and the computing times in such a simulation are enormous. For example, the eight 7-day arcs result in eight normal matrices with a total size of 220 Megabytes, and forming one normal matrix requires 3 CPU hours on a Pentium-III 600 MHZ machine. The random errors are generated using "gasdev" and "ran1" from *Numerical Recipes* (Press et al. 1989) with a given standard deviation (3 cm in the case of COSMIC). The random errors are normally distributed. The choice of a 1-minute interval is based on the assumption that the shortest wavelength of the gravity field that COSMIC can sense corresponds to a degree-50 field (the actual maximum degree can be higher). At 800 km, a COSMIC satellite will take about 6050 seconds to travel in one revolution. According to the sampling theorem (see e.g. Meskó 1984), the along-track sampling interval should be $6050/(2 \times 50) \approx 60$ seconds. In general, the along-track sampling interval is

$$\Delta t = \frac{T}{2K} \approx \frac{\pi a^{3/2}}{K\sqrt{GM}} \tag{36}$$

where T is the period of one revolution, K is the maximum degree of the geopotential field [see Eq. (14)] used in the orbit integration, and a is the semi-major axis of the mean orbital ellipse. However, to be compatible with the satellite cross-track spacing, the actual along-track sampling interval can be larger than that given in Eq. (36). For example, Chao et al. (2000) used a
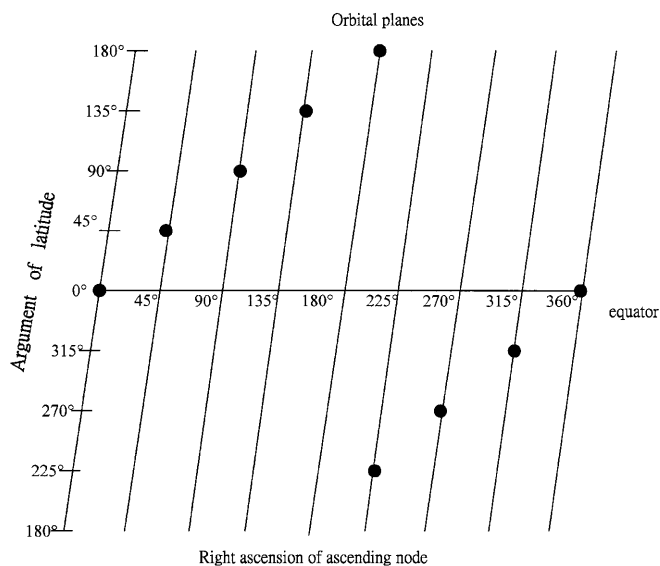

Fig. 5. Configuration of the COSMIC constellation in the operational phase at the initial epoch of orbit integration (0 hour UTC, 1 Jan 2001). The eight satellites are placed on eight orbital planes with evenly spaced right ascensions and arguments of latitude

5-minute interval when deriving normal point data from the geodetic phase of COSMIC.

The recovered coefficients were then assessed by examining the external and internal accuracies. For the external accuracy we computed the relative error of a coefficient by

$$E_{nm}^c = \left| \frac{\Delta\bar{C}_{nm} - \Delta\hat{\bar{C}}_{nm}}{\Delta\bar{C}_{nm}} \right|, \quad E_{nm}^s = \left| \frac{\Delta\bar{S}_{nm} - \Delta\hat{\bar{S}}_{nm}}{\Delta\bar{S}_{nm}} \right| \quad (37)$$

where $\Delta\hat{\bar{C}}_{nm}$ and $\Delta\hat{\bar{S}}_{nm}$ are the estimates of $\Delta\bar{C}_{nm}$ and $\Delta\bar{S}_{nm}$ (the differences between EGM96 and OSU91A coefficients). Figure 6 shows the relative errors of the recovered coefficients. For comparison, the relative errors of the recovered coefficients without weighted constraints are also shown in Fig. 6. Indeed, the constraints have reduced the relative errors considerably. For coefficients of degree lower than 10, the relative errors are mostly below 0.1. The relative errors of the sectorial coefficients are relatively small compared to the errors of other harmonics. Figure 7 shows the relative errors of the recovered zonal coefficients with constraint. In general, the low-degree zonal terms are better determined than the high-degree ones. The $\bar{C}_{2,0}$ term has an error of 0.05, which is almost the smallest among all coefficients.

In particular, the odd zonal coefficients $\bar{C}_{5,0}$, $\bar{C}_{15,0}$, and $\bar{C}_{37,0}$ have very large errors. The result in Fig. 7 shows that, despite the fact that the zonal terms produce orbit variations that are mixed with the 1-cpr terms of the empirical model, they are still well recovered with the help of the weight matrix $\mathbf{P_X}$. The external errors will be
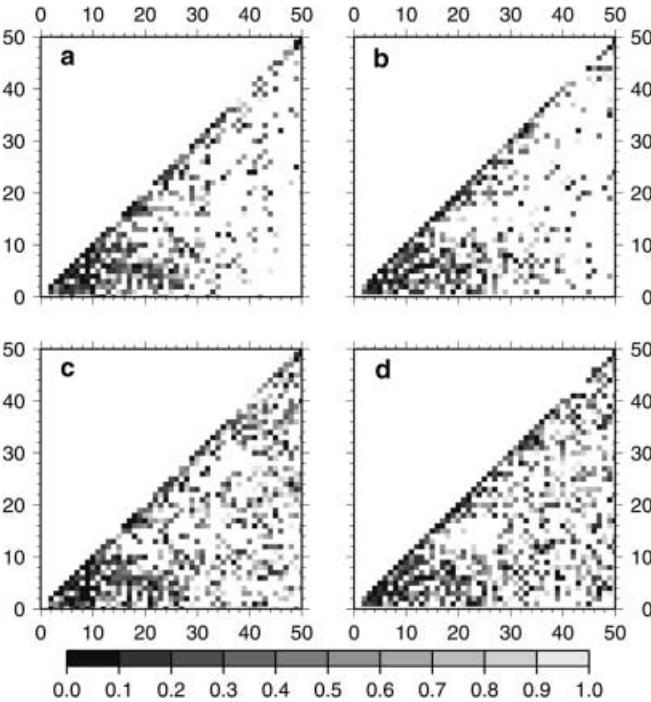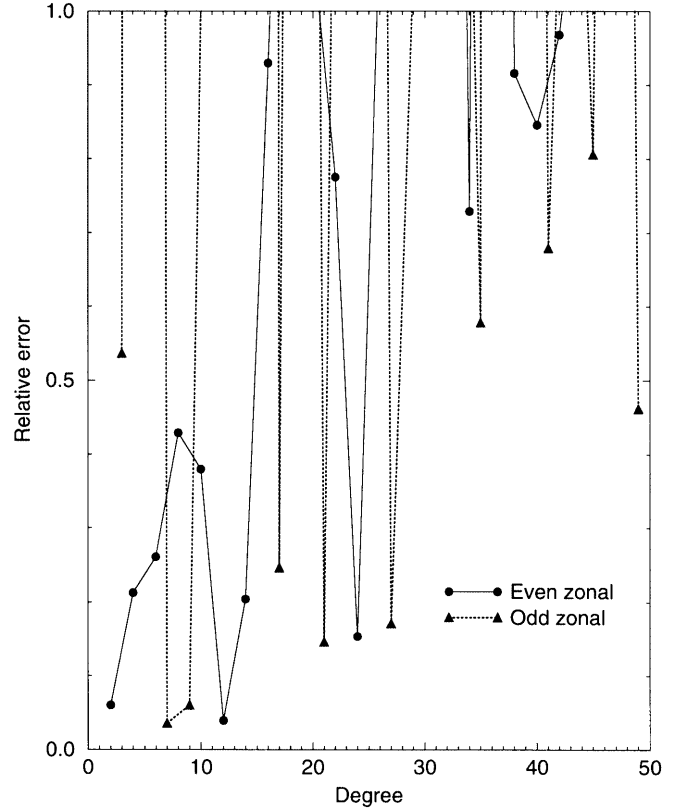

Fig. 7. Relative errors of recovered zonal coefficients from the degree-50 solution with constraint

further reduced if more than 1 week of COSMIC data are used.

Next we examine the internal accuracy using geoid error by degree computed by

$$\varepsilon_n = R_e \sqrt{\sum_{m=0}^{n} \left(\varepsilon_{\bar{C}_{nm}}^2 + \varepsilon_{\bar{S}_{nm}}^2 \right)} \quad (38)$$

where R_e is the Earth's mean radius; $\varepsilon_{\bar{C}_{nm}}$ and $\varepsilon_{\bar{S}_{nm}}$ are the standard errors of $\bar{C}_{nm}$ and $\bar{S}_{nm}$, respectively. Figure 8 shows the geoid errors by degree computed from the recovered field and those from the EGM96 model. In Fig. 8 we also show the geoid errors from a 1-year solution, which are extrapolated using the empirical formula: error from 1-year solution = error from 1-week solution/$\sqrt{52}$. (This formula has been verified by the result: error from eight-satellite solution = error from one-satellite solution/$\sqrt{8}$, see also Wahr et al. 1998.) As shown in Fig. 8, below degree 7 the geoid errors from the 1-week solution of COSMIC are comparable to that from EGM96, and beyond degree 7 the former are larger than the latter. However, for degrees below 26 the geoid error from the 1-year solution is much smaller than that from EGM96. With 5 years of COSMIC data, improvement at degrees higher than 26 can be foreseen. On the other hand, improvement at higher degrees can be achieved by using the geodetic phase data of COSMIC that spans a relatively short time, since the gravity signal-to-noise
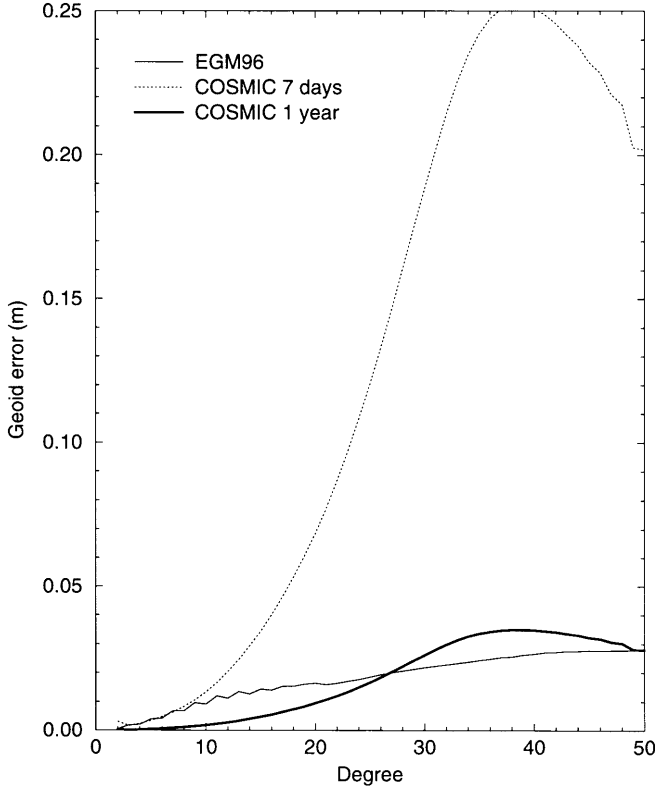

Fig. 6. Relative errors of the recovered harmonic coefficients from the degree-50 solution for **a** $\Delta\hat{\bar{C}}_{nm}$ without constraint, **b** $\Delta\hat{\bar{S}}_{nm}$ without constraint, **c** $\Delta\hat{\bar{C}}_{nm}$ with constraint, and **d** $\Delta\hat{\bar{S}}_{nm}$ with constraint

Fig. 8. Geoid errors by degree computed from the coefficient errors of the EGM96 model, and the models from the COSMIC solutions using 7 days and 1 year of data

ratio will be significantly magnified due to the lower altitude (Chao et al. 2000).

5.2. Recovering temporal gravity variation

5.2.1 Generating gravity variation due to oceanic mass variation

Next we wish to study the performance of COSMIC in recovering temporal gravity variation. The operational phase of COSMIC may last as long as 5 years, so its data are ideal for determining temporal gravity variation, which is due to factors such as changes in oceanic mass, atmospheric mass, ground-water level, and ice-sheet thickness; see also Chao (1993) and Wahr et al. (1998) for useful discussions on this issue. In comparison to the Earth's static gravity, the temporal gravity variation is very small and is further reduced at satellite altitude. In this simulation, we assume that the only source of gravity variation arises from the variation in the oceanic mass as observed by T/P. T/P is a satellite altimeter mission specifically designed to measure sea surface heights (SSHs); see also Fu et al. (1994) for a complete description of this mission. Note that, according to Wahr et al. (1998), for the annual component, the largest geoid variation is due to the continental water variation, then the atmosphere, and finally the oceans. As the parameters to be recovered, we generate spherical harmonic coefficients of gravity variation as follows.

(1) Average 5.6 years of T/P altimeter data to obtain mean SSHs.
(2) Compute the difference between the SSH of T/P Cycle 196 and the mean SSH. The difference is called sea level anomaly (SLA).
(3) Compute the steric anomaly in January 1994 (the month of T/P Cycle 196) (see Appendix B).
(4) Subtract the steric anomaly from SLA, yielding corrected SLA (CSLA).
(5) Compute the spherical harmonic coefficients of the potential due to the mass of CSLA up to degree 180 (see Appendix C).

The steric anomaly due to thermal expansion of the oceans will not cause mass variation, so it must be removed from the raw SLA in order to see the temporal, oceanic mass variation. Figure 9 shows SLA and CSLA from T/P Cycle 196, and the steric anomaly, and Table 3 shows their statistics. Cycle 196 is selected to see the large variation of SSH over the Pacific Ocean and the Indian Ocean during the 1997–1998 El Niño. By comparing the RMS values of SLA and the steric anomaly in Table 3, we find that globally the steric anomaly contributes about half of the sea level variation. As seen in Fig. 9, the sea surface northeast of Australia dropped by as much as 20 cm, while the sea surface in the central, eastern Pacific rose by about the same amount. The sea surface northeast of Madagascar also rose by more than 20 cm. These lows and highs in the sea surface are the result of the 1997–1998 El Niño, and only partially due to the steric anomaly (we can compare the SLA and CSLA maps to see this). That is, during the 1997–1998 El Niño, there were actual large mass variations northeast of Australia and in the central, eastern Pacific. Figure 10 shows the degree amplitudes of the geoid variation due to the mass variation. Degree amplitude of geoid is defined as

$$N_n = R_e \sqrt{\sum_{m=0}^{n} (\bar{J}_{nm}^2 + \bar{K}_{nm}^2)} \qquad (39)$$

where $\bar{J}_{nm}$ and $\bar{K}_{nm}$ are the harmonic coefficients of the gravity variation; and R_e is defined in Eq. (38). For the CSLA-induced geoid variation, all degree amplitudes are smaller than 1 mm, except at degrees 2 and 3. Thus the geoid variation is indeed very small compared to the total geoid (about 30 m RMS from EGM96 to degree 360). Also shown in Fig. 10 is the cumulative percentage power up to degree L, defined as

$$P_L = \frac{\sum_{n=2}^{L} N_n^2}{\sum_{n=2}^{N_{\max}} N_n^2} \times 100 \qquad (40)$$

where $N_{\max}$ is the highest degree of expansion, which is 180 in this case. Based on Fig. 10, the power of the geoid variation is concentrated at the low-degree terms. For example, up to degrees 5, 10, 15, 36, and 50, the cumulative percentage powers are 84.5, 96.8, 98.8, 99.8, and 99.9%, respectively. Figure 11 shows the geoid variations expanded to degrees 5, 15, and 50. At as low as degree 5, the signatures of geoid variation over the
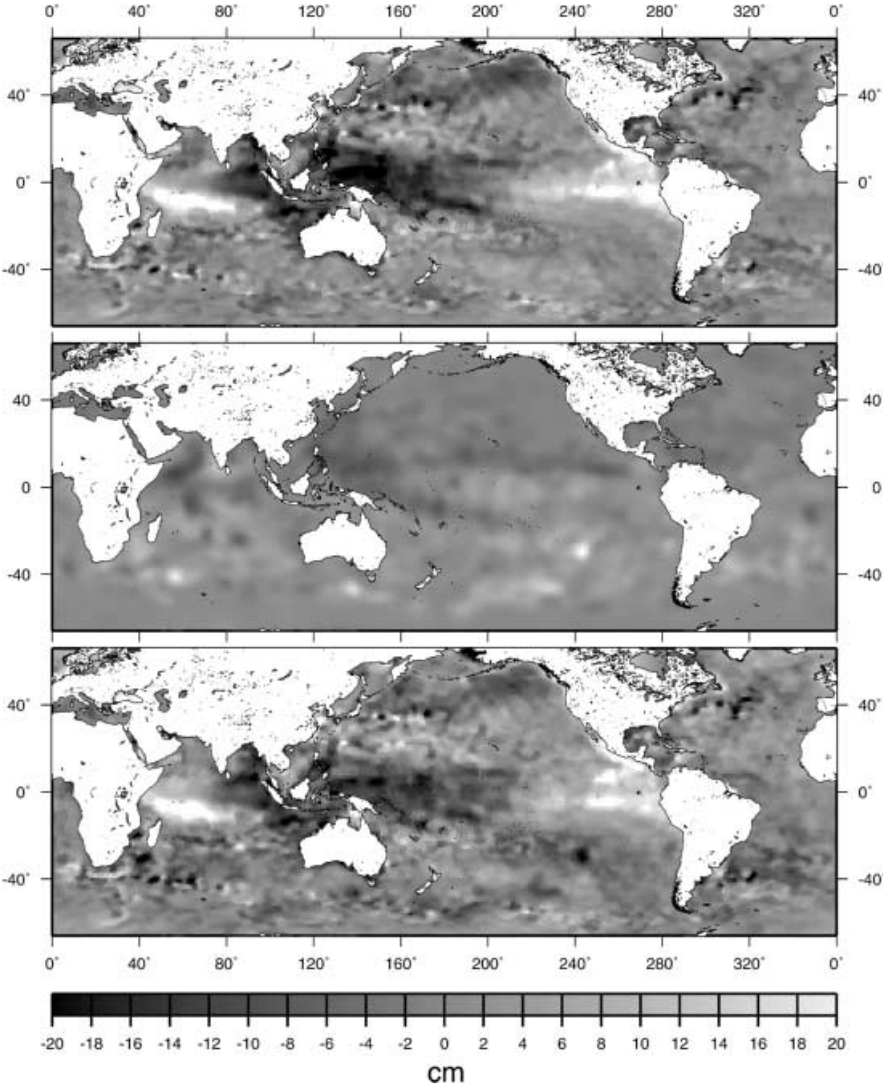
Fig. 9. TOPEX/POSEIDON-observed raw sea level anomaly (**top**), temperature-derived steric anomaly (**center**), and corrected sea level anomaly (by steric anomaly) (**bottom**) at Cycle 196

Table 3. Statistics of sea level anomaly, steric anomaly and corrected sea level anomaly (in cm) over oceans with depth greater than 500 m

	Maximum	Minimum	Mean	RMS
Sea level anomaly	29.9	−54.4	0.22	5.4
Steric anomaly	21.41	−11.61	0.32	2.5
Corrected sea level anomaly	38.4	−47.9	−0.1	5.3

Pacific Ocean and the Indian Ocean are still apparent and are consistent with those of CSLA in Fig. 9. Specifically, in the western Pacific a negative CSLA results in a mass deficiency, which then causes a negative geoid variation there; in the eastern Pacific, the sign of CSLA is reversed, leading to a positive geoid variation there. During the 1997–1998 El Niño the largest geoid change occurred around the Galapagos Islands and exceeded 1 cm. Furthermore, by LS fitting an expression $\alpha n^{-\beta}$ to the averaged degree variances of the gravity variation, we find

$$\bar{\tau}_n^2 = \frac{1}{2n+1} \sum_{m=0}^{n} (\bar{J}_{nm}^2 + \bar{K}_{nm}^2) \approx 7 \times 10^{-19} n^{-4} \qquad (41)$$

Figure 12 compares the modeled and true degree variances of the gravity variation. Comparing the expressions in Eqs. (34) and (41), we find

$$\bar{\sigma}_n \approx 10^4 \bar{\tau}_n \qquad (42)$$

Thus at any degree the static gravity signals (e.g. geoid undulation, gravity anomaly, deflection of the vertical, etc.) are about 10 000 times larger than the temporal gravity signals due to oceanic mass variation.

5.2.2 Recovery
Now we attempt to recover the geoid variation in Fig. 11 from the COSMIC data. In this simulation, we assume that EGM96 is the true, static gravity field determined from dedicated gravity missions such as GRACE, CHAMP, and GOCE (Balmino et al. 1998). The time-dependent gravity field is then the sum of EGM96 implied static gravity and the change of gravity.
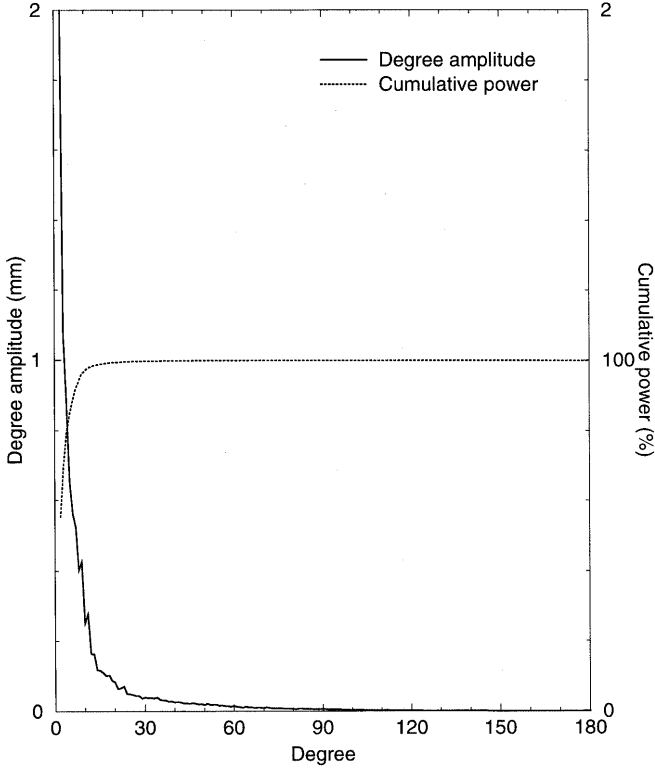
Fig. 10. Degree amplitude and cumulative percentage power of geoid variation computed from the corrected sea level anomaly in Fig. 9

Let $\bar{C}_{nm}^E$ and $\bar{S}_{nm}^E$ be the geopotential coefficients of EGM96. The steps of simulation are as follows.

(1) Compute $\bar{C}_{nm}^T = \bar{C}_{nm}^E + \bar{J}_{nm}$ and $\bar{S}_{nm}^T = \bar{S}_{nm}^E + \bar{K}_{nm}$.

(2) Integrate 7-day orbits at a 1-minute interval using $\bar{C}_{nm}^T$ and $\bar{S}_{nm}^T$ up to degree 50 for each of the eight COSMIC satellites. Random errors are added to the orbits based on a 3-cm standard deviation. These orbits are treated as positional data of COSMIC.

(3) Repeat (2), but with $\bar{C}_{nm}^E$ and $\bar{S}_{nm}^E$ and without random errors.

(4) Subtract the orbits in (3) from the orbits in (2) to obtain the radial, along-track, and cross-track perturbations due to mass variation.

(5) Compute $\hat{\bar{J}}_{nm}$ and $\hat{\bar{K}}_{nm}$, which are the estimates of $\bar{J}_{nm}$ and $\bar{K}_{nm}$, by LS using the linear perturbation theory with data from the "observed" perturbations in (4).

Figure 13 shows the perturbations of a COSMIC satellite orbit due to the mass variation (note: no noises are added to these perturbations). If the higher-order and resonance effects are removed, the RMS values of the radial, along-track, and cross-track perturbations are only 0.4, 4.5, and 1.2 cm, respectively, which are very small and can easily be obscured by GPS noises. In the LS estimation we have tried three different solutions: the first solution does not use any weighted constraints, the second solution uses constraints based on the static degree variances in Eq. (34), and the third solution uses constraints based on the temporal degree variances in Eq. (41).

The first and second solutions result in recovered coefficients that are too large to produce any meaningful structures of geoid variation. The third solution, however, yields a convincing result. Figure 14 shows the relative errors of the recovered coefficients from the third solution. Up to degree 18 the sectorial harmonics are best recovered and the low-degree terms have relatively small errors. For most of the coefficients, the relative errors are below 1, indicating that the COSMIC satellites can sense harmonic coefficients up to as high as degree 50 (assuming that the static gravity is accurate up to degree 50). Figure 15 shows the recovered geoid variations up to degrees 5, 15, and 50. Due to the GPS noises and the polar gaps in the data coverage, the true geoid variations in Fig. 11 cannot be fully recovered. In addition, a surface signal such as geoid variation will be attenuated at satellite altitude, making a full recovery of the signal even more difficult. In fact, beyond degree 15 the resolution of the recovered geoid variation does not improve at all. We also tried a solution using 1 month of COSMIC data, but the result is not improved and is almost identical to that from 1 week of data. However, important signatures of the temporal gravity variation are retained in the recovered fields. For example, the geoid lows northeast of Australia and in the Atlantic Ocean, and the geoid highs near the Galapagos Islands and east of Madagascar are clearly seen in Fig. 15. Based on this experiment, we conclude that, given data noise of 3 cm at a 1-minute interval, COSMIC is able to see temporal gravity variation on a time scale of at least 1 week and on a spatial scale of about 2600 km (the equivalent scale of degree 15), under the conditions that the static gravity is very accurate and the orbital perturbations arising from other time-varying forces are properly modeled.

5.2.3 The effects of data noise and mismodeled perturbing forces on recovering temporal gravity

The result in the above experiment has shown that we cannot fully recover the temporal gravity variation with a 3-cm noise in the COSMIC data. To understand more about how the noise of COSMIC data will affect the result, we generated 7 days of orbit for each of the eight COSMIC satellites using degree-50 fields in the orbit integrations, as in the previous section. However, here we used three different noises in the "observed" perturbations: 3, 1, and 0.1 cm. The "observed" perturbations were then used to compute the temporal gravity variations up to degree 15. The reasons for using the degree-15 solutions are: (1) to avoid aliasing into low-degree terms from the high-degree terms due to the polar gaps; (2) to avoid using a priori weighted constraints of any kind; and (3) to avoid singularity in the normal matrix in the case of no constraints. Figure 16 shows the relative errors from using the three noises. Clearly the relative error decreases as the noise decreases. The result from the case with noise equal to 3 cm is almost identical to the result from the degree-50 solution (up to degree 15) described in the previous section. The best result is with noise equal to 0.1 cm, and the recovered geoid variations up to degrees 5, 10, and 15 are shown in Fig. 17. The degree-10 geoid in Fig. 17 closely resembles the degree-15 geoid in
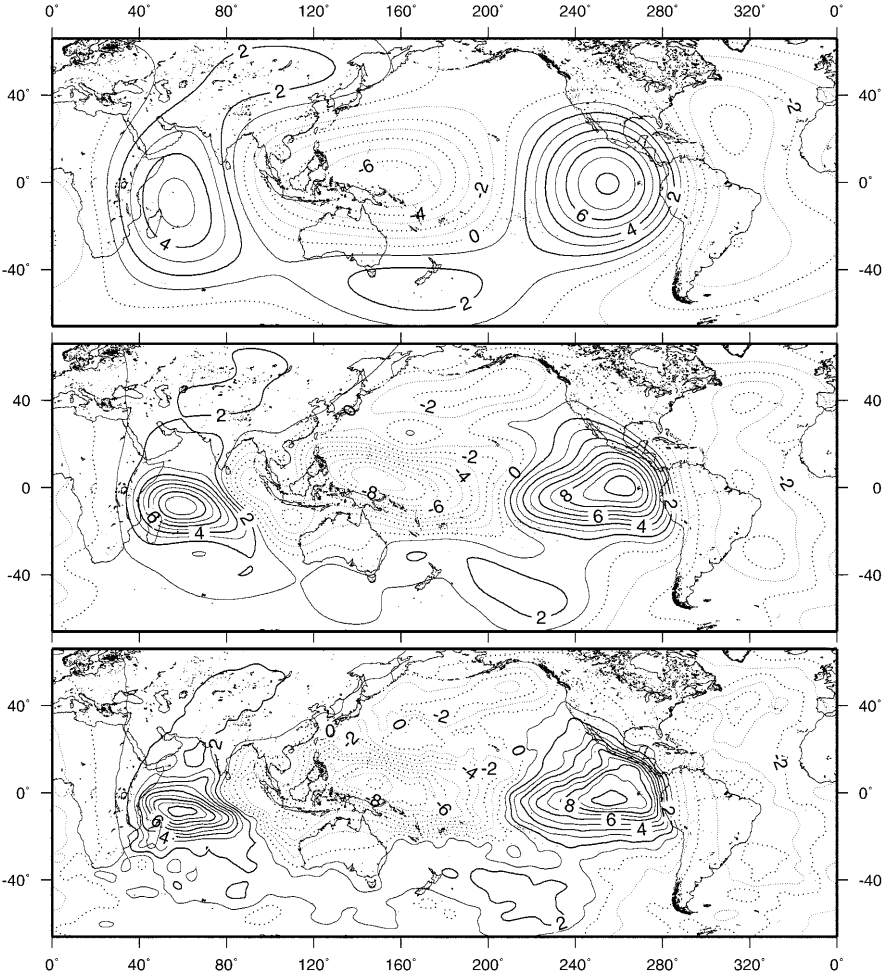
Fig. 11. Contour maps of geoid variation up to degrees 5 (**top**), 15 (**center**), and 50 (**bottom**) from the corrected sea level anomaly in Fig. 9. Unit is mm

Fig. 11. In the case of 0.1-cm noise, the degree-15 geoid improves the resolution over the degree-10 geoid, but the former contains some artifacts, for example the distorted geoid variations in the eastern Pacific and in the central Atlantic. We also find that the degree-5 geoid from the case with noise equal to 1 cm (not plotted here) agrees very well with the degree-5 geoid in Fig. 11. This experiment suggests that the noise of COSMIC data has a substantial impact on the achievable resolution in the recovered gravity variation. Furthermore, it appears that the polar gaps in the COSMIC orbits will not do too much damage to the low-degree solutions performed here, but it is expected that the accuracy of recovery will be improved if the COSMIC satellites are in polar orbits.

In previous sections we have pointed out the importance of modeling perturbing forces in recovering temporal gravity variation from tracking data such as COSMIC's. In theory, in order to evaluate the impact of mismodeled perturbing forces on recovered temporal gravity variation, we can add systematic and random errors to each of the given force models and see what kind of damage the errors will do to the recovered signals. Such an experiment can be done using software like NASA's GEODYN (Pavlis et al. 1996). Here we present just a simplified discussion using STARLETTE's orbit. For STARLETTE, whose altitude is about 966 km, the magnitudes of accelerations due to selected perturbing forces are as given in Table 4 (Reigber 1989). Compared to the geopotential, the accelerations due to other forces are relatively small. We now calculate average acceleration by degree (Hwang and Lin 1998) due to the oceanic mass movement (derived from T/P as in this paper) by

$$a_n = \sqrt{\left(\frac{GM}{r^2}\right)^2 \left(\frac{a_e}{r}\right)^{2n} (n+1)(2n+1) \sum_{m=0}^{n} (\bar{J}_{nm}^2 + \bar{K}_{nm}^2)}$$

(43)

where r is the average geocentric distance to COSMIC (about 7171 km), and the $\bar{J}_{nm}, \bar{K}_{nm}$ coefficients are defined in Eq. (39). Figure 18 shows the average accelerations by degree up to degree 50 due to the oceanic mass variation. In Fig. 18, the errors of accelerations due to mismodeled perturbing forces based on a 1% relative error are also plotted. These errors are assumed to be "flat"; that is, the errors are the same at any harmonic degree. As we can see from Fig. 18, for N-body, Earth tides, and ocean tides, the 1% error is too large for us to see temporal gravity variation up to degree 50 from COSMIC. In order to achieve a degree-50 resolution in temporal gravity variation (due to the oceanic mass variation), the relative errors of N-body, Earth tides, and ocean tides must be smaller than $10^{-5}, 10^{-4}$, and 10^{-3}, respectively.
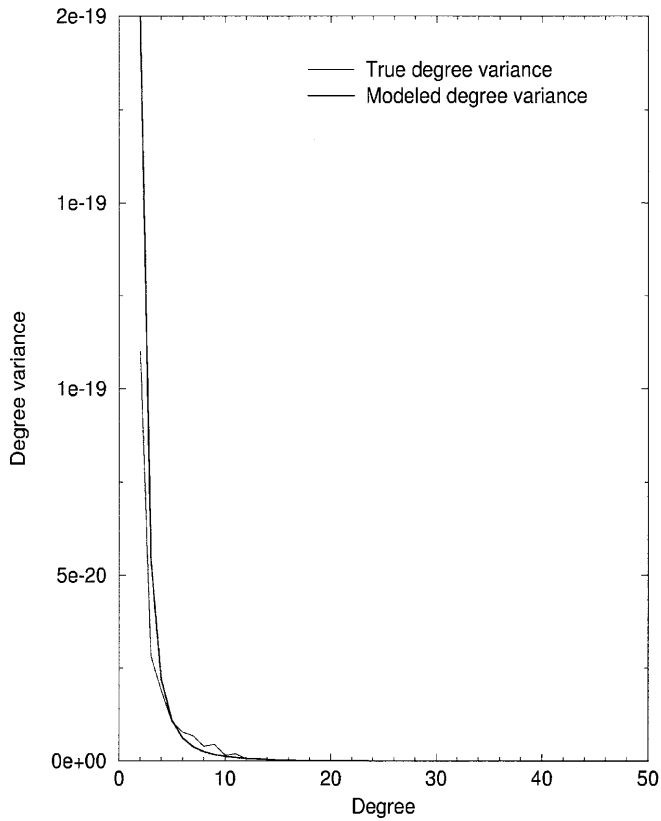
Fig. 12. True and modeled degree variances of gravity variation due to oceanic mass variation

recover gravity fields using the simulated, GPS-derived positional data from the COSMIC mission in the operational phase. Our results show that the COSMIC data can improve the long-wavelength part of the EGM96 model. Most important is that the COSMIC data can be used to recover temporal gravity variations, especially the gravity signatures due to the oceanic mass movement in an El Niño. With a 3-cm noise at a 1-min interval, COSMIC can recovery temporal gravity variation on a time scale of at least 1 week and on a spatial scale of about 2600 km, provided that the static gravity is very accurate and time-varying perturbing forces are properly modeled. However, in order to see more clearly the structure of temporal gravity variation, the noise of COSMIC positional data should be reduced to 1 cm or less at a 1-min interval. Thus, it is necessary to develop a good data processing method for noise reduction. The technique developed here can be applied to gravity recoveries from the data of the CHAMP and GRACE missions, which have onboard accelerometers to measure surface forces. However, like COSMIC, CHAMP and GRACE will face the same problem of modeling such gravitational forces as those from the N-body, ocean tides, and solid-Earth tides. Most of these gravitational forces are time-varying and, if not properly modeled, they will alias into the temporal gravity signals that we wish to recover from the COSMIC, CHAMP, and GRACE data.

Appendix A

Order-zero perturbations

For a satellite orbit with a small eccentricity, we may assume $r = a, f = E = M$ in Eqs. (4), (5), and (6) to obtain the approximations
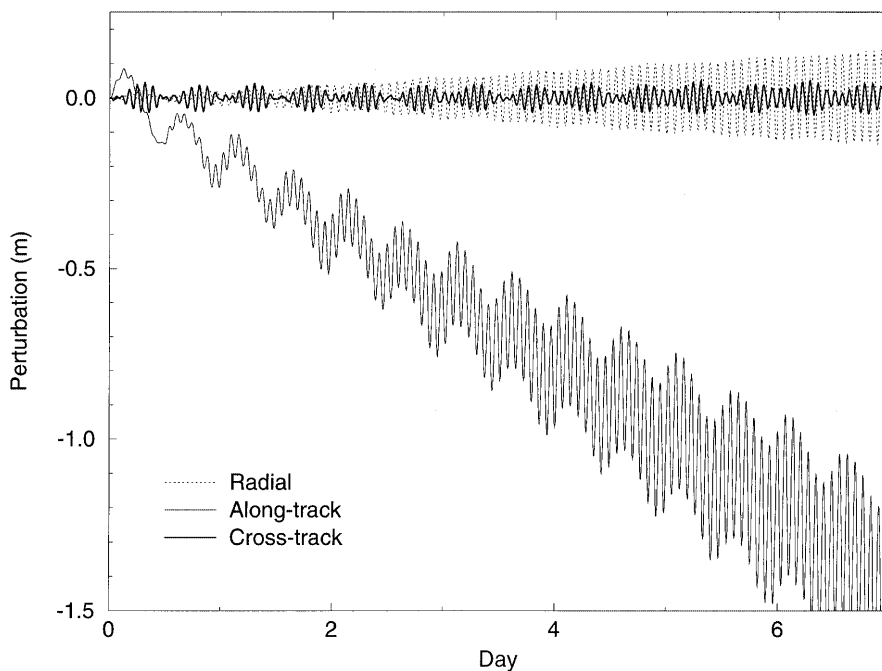
6 Conclusions

In this paper we proposed improved formulas of orbital perturbations, which were then verified by numerical analysis. The perturbation formulas were used to

Fig. 13. Perturbations of COSMIC orbit due to the mass variation of corrected sea level anomaly up to degree 50. Day is the number of days elapsed since the first data point
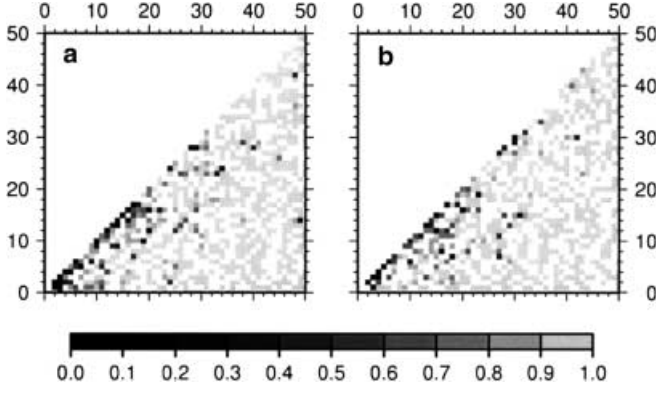
Fig. 14. Relative errors of the recovered harmonic coefficients of gravity variation for **a** $\Delta \hat{\bar{J}}_{nm}$ and **b** $\Delta \hat{\bar{K}}_{nm}$ using 1 week of COSMIC data and degree-50 solution

$$\Delta x_1^0 = (1 - e\cos M)\Delta a - (a\cos M)\Delta e + (ae\sin M)\Delta M \quad (A1)$$

$$\Delta x_2^0 = a[\Delta\omega + \Delta M + (\cos I)\Delta\Omega] \quad (A2)$$

$$\Delta x_3^0 = a[(\sin(\omega + M)\Delta I - (\sin I\cos(\omega + M))\Delta\Omega)] \quad (A3)$$

Furthermore, in Eq. (14) we set $Q = 1$. This truncated series of R will then require only the G_{np0} and $G_{np\pm1}$ terms, which can be approximated as (Balmino 1994, p 270)

$$G_{np0} = 1,$$
$$G_{np1} = \frac{(3n - 4p + 1)e}{2}, \quad (A4)$$
$$G_{np-1} = \frac{(-n + 4p + 1)e}{2},$$

$$G'_{np0} = 0,$$
$$G'_{np1} = \frac{3n - 4p + 1}{2}, \quad (A5)$$
$$G'_{np-1} = \frac{-n + 4p + 1}{2},$$

Substituting Eqs. (A4) and (A5) into Eqs. (20) and (19), and finally into Eqs. (A1), (A2), and (A3), with some trigonometric identities we obtain the order-zero perturbations

$$\Delta x_1^0 = \sum_{n=2}^{K} \sum_{m=0}^{n} \sum_{p=0}^{n} C_{nmp}^1 S_{nmp0} \quad (A6)$$
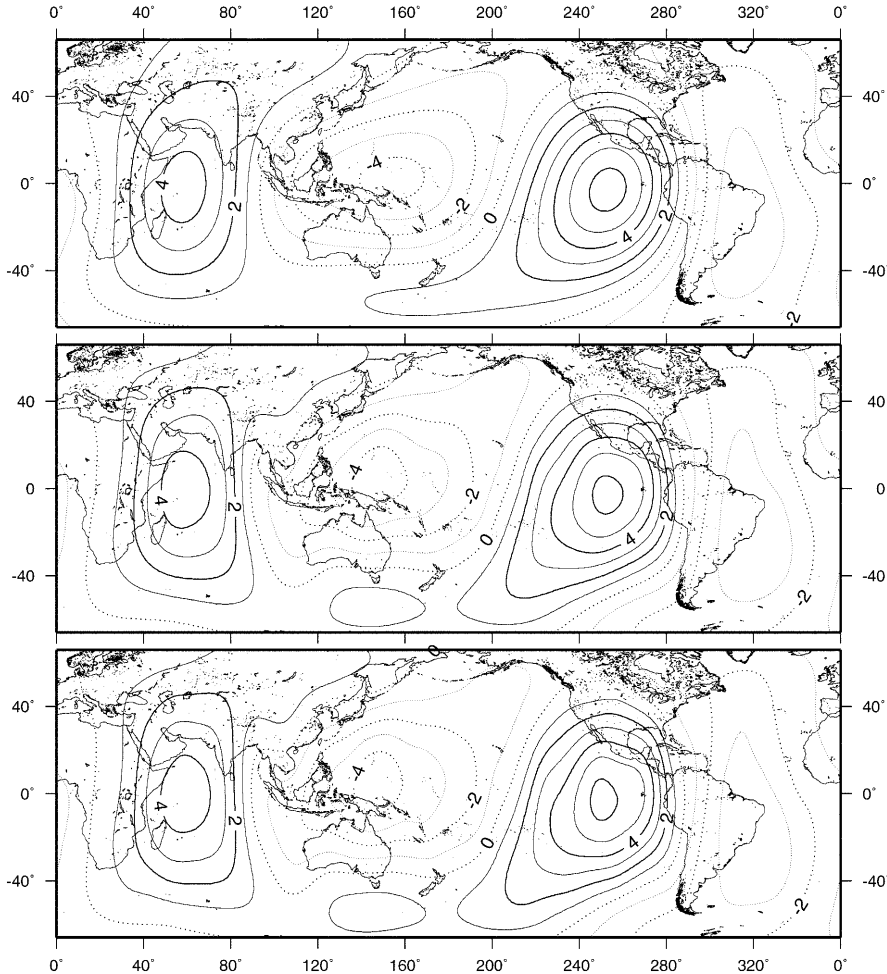

Fig. 15. Contour maps of recovered geoid variation up to degrees 5 (**top**), 15 (**center**), and 50 (**bottom**) using 1 week of COSMIC data and degree-50 solution. Unit is mm
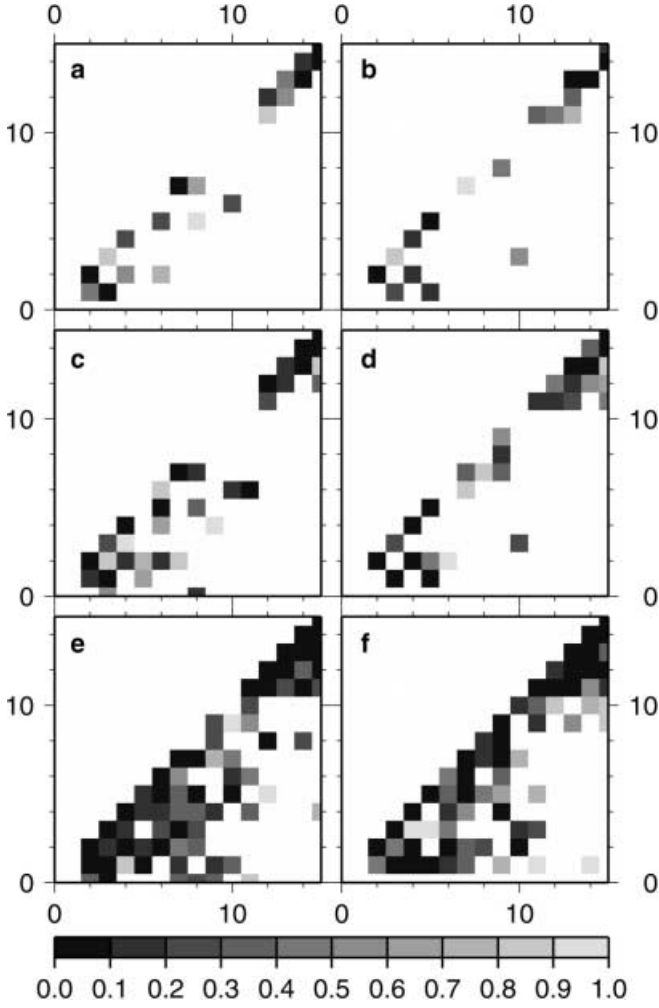
Fig. 16. Relative errors of the recovered harmonic coefficients of gravity variation using 1 week of COSMIC data and degree-15 solutions for **a** $\Delta\hat{\bar{J}}_{nm}$ (3-cm noise), **b** $\Delta\hat{\bar{K}}_{nm}$ (3-cm noise), **c** $\Delta\hat{\bar{J}}_{nm}$ (1-cm noise), **d** $\Delta\hat{\bar{K}}_{nm}$ (1-cm noise), **e** $\Delta\hat{\bar{J}}_{nm}$ (0.1-cm noise), and **f** $\Delta\hat{\bar{K}}_{nm}$ (0.1-cm noise)

$$\Delta x_2^0 = \sum_{n=2}^{K}\sum_{m=0}^{n}\sum_{p=0}^{n} C_{nmp}^2 S_{nmp0}^* \tag{A7}$$

$$\Delta x_3^0 = \sum_{n=2}^{K}\sum_{m=0}^{n}\sum_{p=0}^{n} (C_{nmp}^{3-} S_{(n+1)mp0}^* - C_{nmp}^{3+} S_{(n-1)mp0}^*) \tag{A8}$$

where

$$C_{nmp}^1 = \bar{n}a\left(\frac{a_e}{a}\right)^n \bar{F}_{nmp}\left[\frac{2(n-2p)}{\dot{\psi}_{nmp0}} + \frac{-3n+4p-1}{2\dot{\psi}_{nmp1}}\right.$$
$$\left. + \frac{-n+4p+1}{2\dot{\psi}_{nmp-1}}\right] \tag{A9}$$

$$C_{nmp}^2 = \bar{n}a\left(\frac{a_e}{a}\right)^n \bar{F}_{nmp}\left[\frac{2(n+1)-3(n-2p)\bar{n}/\dot{\psi}_{nmp0}}{\dot{\psi}_{nmp0}}\right.$$
$$\left. + \frac{-3n+4p-1}{\dot{\psi}_{nmp1}} + \frac{n-4p-1}{\dot{\psi}_{nmp}}\right] \tag{A10}$$

$$C_{nmp}^{3\pm} = \frac{a}{2}\left(\frac{a_e}{a}\right)^n \frac{\bar{n}}{\dot{\psi}_{nmp0}}\left\{[(n-2p)\cos I - m]\frac{\bar{F}_{nmp}}{\sin I} \mp \bar{F}_{nmp}'\right\} \tag{A11}$$

$$S_{(n\pm1)mp0}^* = \begin{bmatrix} \bar{C}_{nm}^+ \\ -\bar{S}_{nm}^- \end{bmatrix}\sin\psi_{(n\pm1)mp0} - \begin{bmatrix} \bar{S}_{nm}^+ \\ -\bar{C}_{nm}^- \end{bmatrix}\cos\psi_{(n\pm1)mp0} \tag{A12}$$

This result can also be found in Rosborough and Tapley (1987).

Appendix B

Computation of steric anomaly due to thermal expansion

The steric anomaly is sea level variation due to the expansion or contraction of sea water as a result of temperature variations over the entire column of the oceans. However, the upper layers of the oceans contribute most to the steric anomaly. In practice we take into account the contributions from the upper 14 oceanic layers when computing the steric anomaly.

$$\Delta H_S = \sum_{i=1}^{14} \alpha_i \Delta T_i H_i \tag{B1}$$

where α_i is the coefficient of thermal expansion from Gill (1982, Table A3.1); ΔT_i is the temperature anomaly relative to the mean of layer i and H_i is the thickness of layer i; see also Chen et al. (2000, Table 1) for a list of depths and thicknesses of the 14 layers. We obtained via the Internet the monthly, $1° \times 1°$ gridded temperature data at different depths from the Integrated Global Ocean Services System (IGOSS) at Columbia University (see the web site: http://lola.ldgo.columbia.edu/SOURCES/.LEVITUS94). Then, for each of the 14 layers, the mean temperature was determined and subtracted from the raw temperature to obtain the temperature anomaly ΔT_i. It turns out that the quality of temperature data varies over space and time, so we use a medium filter with a 300-km wavelength to filter the computed steric anomaly. Ideally, in this study we should compute the steric anomaly at the mean time of T/P Cycle 196, but the current maximum resolution of reliable global temperature data at different depths is probably only 1 month.

Appendix C

Harmonic coefficients and geoid variation from corrected sea level anomaly

Steric anomaly-corrected sea level anomaly (CSLA) from satellite altimetry includes the deviation of the
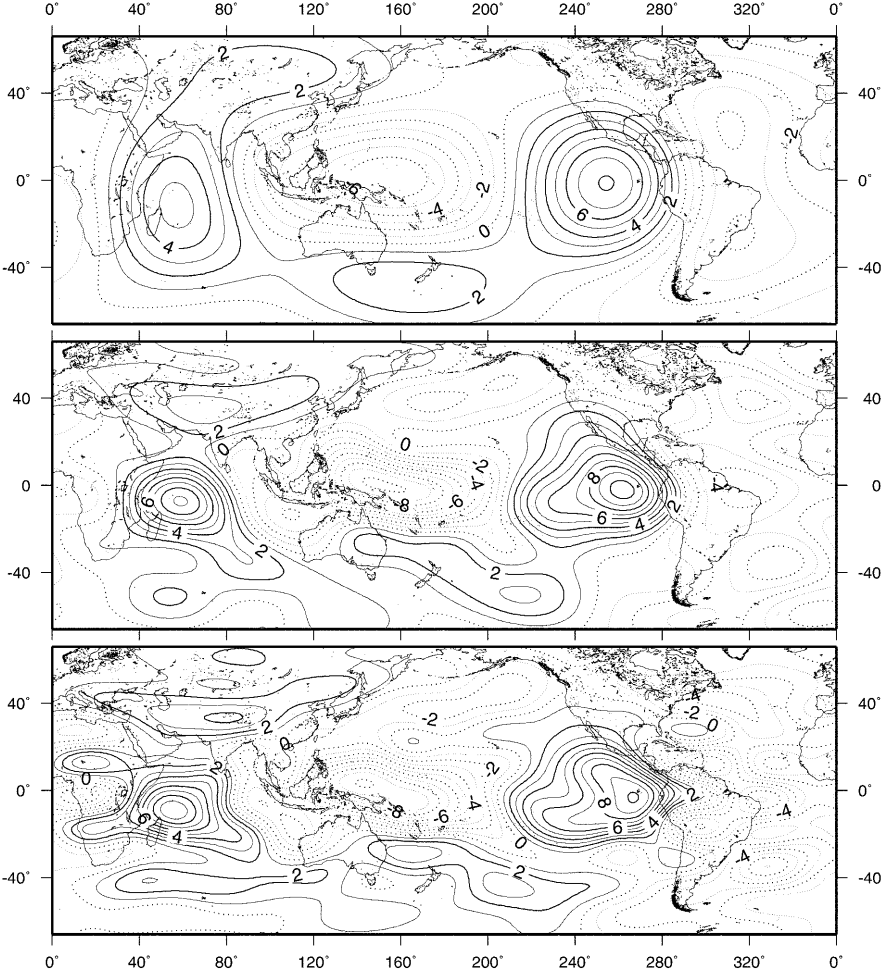
Fig. 17. Contour maps of recovered geoid variation up to degrees 5 (**top**), 10 (**center**), and 15 (**bottom**) using 1 week of COSMIC data and degree-15 solution with noise = 0.1 cm. Unit is mm

Table 4. Magnitudes of accelerations for STARLETTE orbit (from Reigber 1989)

Source of acceleration	Magnitude of acceleration (m s^{-2})
Central term (GM/r)	7.4
C_{20}	8×10^{-3}
Other harmonics of geopotential	1×10^{-4}
N-body	1×10^{-6}
Earth tides	2×10^{-7}
Ocean tides	3×10^{-8}
Atmospheric drag	$1-2 \times 10^{-10}$
Albedo pressure	5×10^{-9}
Solar radiation pressure	5×10^{-10}

instantaneous sea surface (after removing ocean tide and other geophysical effects) from a mean sea surface, and the vertical loading deformation due to the mass of such a deviation. CSLA in this case may be expanded into a series of spherical harmonics as

$$\Delta h(\theta, \lambda)$$
$$= \sum_{n=0}^{K} (1 + k_n) \sum_{m=0}^{n} [\bar{a}_{nm} \bar{R}_{nm}(\theta, \lambda) + \bar{b}_{nm} \bar{S}_{nm}(\theta, \lambda)] \quad (C1)$$

where k_n is the elastic Love number of degree n (for their numerical values, see e.g. Wahr et al. 1998); $\bar{R}_{nm} = \bar{P}_{nm} \cos m\lambda$ and $\bar{S}_{nm} = \bar{P}_{nm} \sin m\lambda$ are fully normalized spherical harmonics [Heiskanen and Moritz 1985; see also Eq. (1)]. The coefficients $\bar{a}_{nm}$ and $\bar{b}_{nm}$ are harmonic coefficients of CSLA without loading effect, and can be obtained by the integrations

$$(1 + k_n) \left\{ \begin{array}{c} \bar{a}_{nm} \\ \bar{b}_{nm} \end{array} \right\}$$
$$= \left\{ \begin{array}{c} \bar{a}'_{nm} \\ \bar{b}'_{nm} \end{array} \right\} = \frac{1}{4\pi} \int_{\theta=0}^{\pi} \int_{\lambda=0}^{2\pi} \Delta h \left\{ \begin{array}{c} \bar{R}_{nm} \\ \bar{S}_{nm} \end{array} \right\} \sin \theta \, \mathrm{d}\theta \, \mathrm{d}\lambda \quad (C2)$$

At any point exterior to the Earth, the potential due to the mass of Δh is

$$\Delta V(r, \theta, \lambda) = R_\mathrm{e} G \rho_\mathrm{w} \int_{\theta'=0}^{\pi} \int_{\lambda'=0}^{2\pi} \frac{\Delta h}{s} \sin \theta' \, \mathrm{d}\theta' \, \mathrm{d}\lambda' \quad (C3)$$

where $\rho_\mathrm{w} \approx 1.03 \, \mathrm{g \, cm^{-3}}$ is the density of sea water, $R_\mathrm{e} \approx 6371$ km is the Earth's mean radius, G is the gravitational constant, and s is the distance between the point at (r, θ, λ) and a mass element. The inverse of s
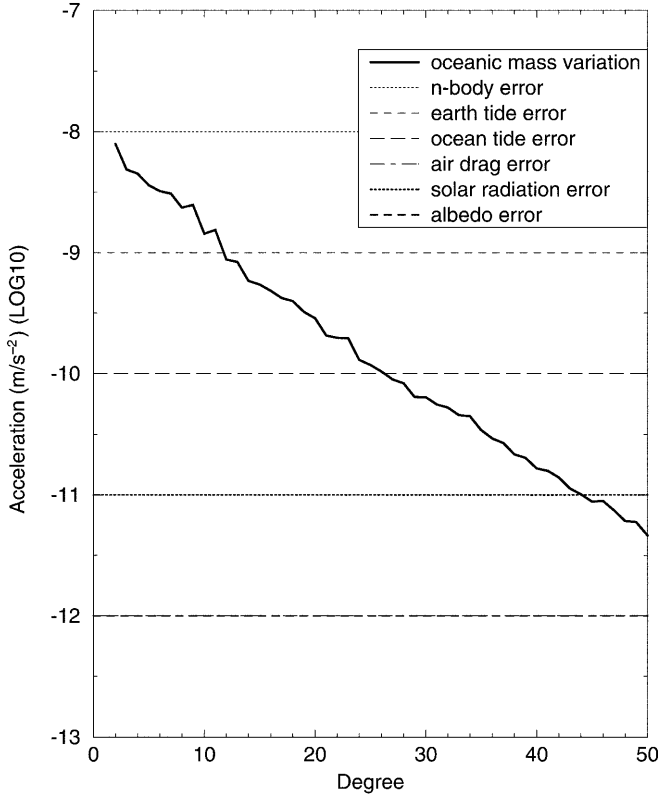
Fig. 18. Average accelerations by degree due to oceanic mass variation and errors of accelerations due to mismodeled perturbing forces based on a 1% relative error from the accelerations listed in Table 4

can be expanded into products of spherical harmonics as (Heiskanen and Moritz 1985)

$$\frac{1}{s} = \frac{1}{r}\sum_{n=0}^{\infty}\frac{1}{2n+1}\left(\frac{R_e}{r}\right)^n\sum_{m=0}^{n}[\bar{R}_{nm}(\theta',\lambda')\bar{R}_{nm}(\theta,\lambda)$$
$$+\bar{S}_{nm}(\theta',\lambda')\bar{S}_{nm}(\theta,\lambda)] \tag{C4}$$

Substituting Eqs. (C4) and (C1) into Eq. (C3), and using the orthogonal relationship of spherical harmonics, we obtain

$$\Delta V(r,\theta,\lambda) = \frac{GM}{r}\sum_{n=0}^{\infty}\left(\frac{R_e}{r}\right)^n$$
$$\times\sum_{m=0}^{n}[\bar{J}_{nm}\bar{R}_{nm}(\theta,\lambda)+\bar{K}_{nm}\bar{S}_{nm}(\theta,\lambda)] \tag{C5}$$

where M is the Earth's mass and

$$\begin{Bmatrix}\bar{J}_{nm}\\\bar{K}_{nm}\end{Bmatrix} = \frac{4\pi\rho_w R_e^2(1+k_n)}{M(2n+1)}\begin{Bmatrix}\bar{a}_{nm}\\\bar{b}_{nm}\end{Bmatrix}$$
$$= \frac{4\pi\rho_w R_e^2}{M(2n+1)}\begin{Bmatrix}\bar{a}'_{nm}\\\bar{b}'_{nm}\end{Bmatrix} \tag{C6}$$

Thus the elastic Love numbers are canceled out. The harmonic coefficients of ΔV differ from those of CSLA by only a scale factor. Let $C_{nm} = (\bar{a}'_{nm} + \bar{b}'_{nm})$, where

$i = \sqrt{-1}$. Given Δh on a regular $\Delta\theta \times \Delta\lambda$ grid, Eq. (C2) can be approximated as

$$C_{nm} = \frac{1}{4\pi q_n}\sum_{k=0}^{M-1}\sum_{l=0}^{N-1}\Delta\bar{h}(\theta_k,\lambda_l)$$
$$\times\left[\int_{t_k}^{t_{k+1}}\bar{P}_{nm}(t)dt\right]\left[\int_{\lambda l}^{\lambda l+1}e^{-im\lambda}d\lambda\right]$$
$$= \frac{g_m}{4\pi q_n}\sum_{k=0}^{M-1}I\bar{P}_{nm}^k\sum_{l=0}^{N-1}\Delta\bar{h}(\theta_k,\lambda_l)e^{i2\pi ml/N} \tag{C7}$$

where $t_k = \cos(k\Delta\theta)$, $\lambda_l = l\Delta\lambda$, $I\bar{P}_{nm}^k$ is the integration of the associated Legendre function (Paul 1978), q_n is a smoothing factor defined by Rapp (1989 p 266), and

$$g_m = \begin{cases}\Delta\lambda, & \text{if } m=0 \\ [\sin(m\Delta\lambda)-i(\cos(m\Delta\lambda)-1)]/m, & \text{if } m\neq 0\end{cases} \tag{C8}$$

$$\Delta\bar{h}(\theta_k,\lambda_l) = \frac{1}{4}[\Delta h(\theta_k,\lambda_l)+\Delta h(\theta_{k+1},\lambda_l)$$
$$+\Delta h(\theta_k,\lambda_{l+1})+\Delta h(\theta_{k+1},\lambda_{l+1})] \tag{C9}$$

Thus $\Delta\bar{h}$ is the simple mean of four neighboring point values. The expression

$$\sum_{l=0}^{N-1}\Delta\bar{h}(\theta_k,\lambda_l)e^{i2\pi ml/N}$$

in Eq. (C7) can be computed efficiently by fast Fourier transform. With C_{nm} computed, $\bar{a}'_{nm}$ and $\bar{b}'_{nm}$ are simply taken from its real and imaginary parts, respectively.

The geoid variation due to Δh is simply computed by Brun's formula $\Delta N = \Delta V/\gamma$, where γ is normal gravity. At sea level, we can set $r = R_e$ and $\gamma = GM/R_e^2$ to obtain the geoid variation by

$$\Delta N(\theta,\lambda) = R_e\sum_{n=0}^{\infty}\sum_{m=0}^{n}[\bar{J}_{nm}\bar{R}_{nm}(\theta,\lambda)+\bar{K}_{nm}\bar{S}_{nm}(\theta,\lambda)]$$
$$\tag{C10}$$

The error in such a spherical approximation is very small because the geoid variation is already very small.

References

Balmino G (1994) Orbit choice and the theory of radial orbit error for altimetry. In: Sansó F, Rummel R (eds) Satellite altimetry in geodesy and oceanography. Lecture Notes in Earth Sciences, vol 50. Springer, Berlin Heidelberg New York, pp 244–317

Balmino G, Perosanz F, Rummel R, Sneeuw N, Sünkel H, Woodworth P (1998) European views on dedicated gravity field missions: GRACE and GOCE. ESA rep ESD-MAG-REP-CON-001, European Space Agency

Bertiger WI, et al (1994) GPS precise tracking of TOPEX/PO-SEIDON: results and implications. J Geophys Res 99: 24 449–24 464

Chao BF (1993) The geoid and earth rotation. In: Vaniček P, Christou NT (eds) Geoid and its geophysical interpretations. CRC Press, Boca Raton

Chao BF, Pavlis EC, Hwang C, Liu CC, Shum CK, Tseng CL, Yang M (2000) COSMIC: geodetic applications in improving earth's gravity model. Terr Atm Ocean Sci 11: 365–378

Chen JL, Wilson CR, Eanes JR, Nerem RS (1999) Geophysical interpretation of the observed geocenter variations. J Geophys Res 104: 2683–2690

Chen JL, Shum CK, Wilson CR, Chambers DP, Tapley BD (2000) Seasonal sea level change from TOPEX/POSEIDON observation and thermal expansion. J Geod 73: 638–647

Cheng M, Tapley BD (1999) Seasonal variations in low-degree zonal harmonics of the earth's gravity field from satellite laser ranging observations. J Geophys Res 104: 2667–2681

Colombo O (1984) Altimetry, orbits and tides. NASA TM 86180, Greenbelt, MD

Engelis T (1987) Radial orbit error reduction and sea surface topography determination using satellite altimetry. Rep 377, Department of Geodetic Science and Surveying, The Ohio State University, Columbus

Fu L-L, Christensen EJ, Yamarone CA Jr, Lefebvre M, Menard Y, Dorrer M, Escudier P (1994) TOPEX/POSEIDON mission overview. J Geophys Res 99: 24 369–24 382

Gill AE (1982) Atmosphere–ocean dynamics. Academic Press, New York

Heiskanen WA, Moritz H (1985) Physical geodesy. Reprint, Institute of Physical Geodesy, TU Graz

Hwang C (1995) Orthonormal function approach for Geosat determination of sea surface topography. Mar Geod 18: 245–271

Hwang C, Lin M-J (1998) Fast integration of low orbiter' trajectory perturbed by the earth's non-sphericity. J Geod 72: 578–585

Jekeli C, Garcia R (1996) Direct determination of vehicle acceleration using GPS phase observables. ION 52 Annual Meeting, Cambridge, MA, 19–21 June

Kaula WM (1966) Theory of satellite geodesy. Blaisdell, London

Krogh FT (1974) Changing the stepsize in the integration of differential equations using modified divided differences. In: Dold A, Eckmann B (eds) Proc Conf Numerical Solution of Ordinary Differential Equations. Lecture Notes in Mathematics, vol 362. Springer, Berlin Heidelberg New York, pp 22–71

Kuo YH, Lee LC (1999) A constellation of microsatellites promises to help in a range of geoscience research. EOS Trans AGU 80: 467

Lemoine FG, Kenyon SC, Factor JK, Trimmer RG, Pavlis NK, Chinn DS, Cox CM, Klosko SM, Luthcke SB, Torrence MH, Wang YM, Williamson RG, Pavlis EC, Rapp RH, Olson TR (1998) The Development of Joint NASA GSFC and the National Imagery and Mapping Agency (NIMA) Geopotential Model EGM96. Rep. No. NASA/TP-1998-206861, National Aeronautics and Space Administration, Greenbelt, MD

Meskó A (1984) Digital filtering: applications in geophysical exploration for oil. Pitman, London

Nerem RS, Eanes RJ, Thompson PF, Chen JL (2000) Observations of annual variations of the earth's gravitational field using satellite laser ranging and geophysical models. Geophys Res Lett 27(12): 1783–1786

Paul MK (1978) Recurrence relations for integrals of associated Legendre functions. Bull Geod 52: 177–190

Pavlis DE, et al (1996) GEODYN operational manual, 5 vol. Hughes/STX Corp, Greenbelt, MD

Press WH, Flannery BP, Teukolky SA, Vetterling WT (1989) Numerical recipes. Cambridge University Press, New York

Rapp RH (1989) Combination of satellite, altimetric and terrestrial gravity data. In: Sansó F, Rummel R (eds) Theory of satellite geodesy and gravity field determination. Lecture Notes in Earth Sciences, vol 25. Springer, Berlin Heidelberg New York, pp 261–284

Reigber C (1989) Gravity recovery from satellite tracking data. In: Sansó F, Rummel R (eds) Theory of satellite geodesy and gravity field determination. Lecture Notes in Earth Sciences, vol 25. Springer, Berlin Heidelberg New York, pp 197–234

Rim HJ, Davis GW, Schutz BE (1996) Dynamic orbit determination for the EOS laser satellite (EOS ALT/GLAS) using GPS measurements. J Astron Sci 44: 409–424

Rosborough GW, Tapley BD (1987) Radial, transverse and normal satellite position perturbations due to the geopotential. Celest Mech 40: 409–421

Schrama EJO (1991) Gravity field error analysis: applications of global positioning system receivers and gradiometers on low orbiting platforms. J Geophys Res 96: 20 041–20 051

Tapley BD, Ries JC, Davis GW, Eanes RJ, Schutz BE, Shum CK, Watkins MM, Marshall JA, Nerem RS, Putney BH, Klosko SM, Lutcke SB, Pavlis D, Williamson RG, Zelensky NP (1994) Precise orbit determination for TOPEX/POSEIDON, J Geophys Res 99 (C12): 24405–24419

Wagner CA (1989) Summer school lectures on satellite altimetry. In: Sansó F, Rummel R (eds) Theory of satellite geodesy and gravity field determination. Lecture Notes in Earth Sciences, vol 25. Springer, Berlin Heidelberg New York, pp 285–334

Wahr J, Molenaar M, Bryan F (1998) Time variability of the earth's gravity field: hydrological and oceanic effects and their possible detection using GRACE. J Geophys Res 103: 30 205–30 229

Yunck TP, Liu C-H, Ware R (2000) A history of GPS sounding. Terr Atm Ocean Sci 11: 1–20